Do 3D Dynamic Rupture Models Capture the Variability in Long-Period Velocity Pulses? Insights from the 2023 M_w 7.8 Kahramanmaraş Earthquake

Rachel Preca Trapani[1], Mathilde Marchandon[1], Kadek Hendrawan Palgunadi[3,4], Baoning Wu[2], Ming-Hsuan Yen[5], Fabrice Cotton[5], Alice-Agnes Gabriel[2,1]

[1]Department of Earth and Environmental Sciences, Ludwig-Maximilian-Universität (LMU), Munich, Germany
[2]Scripps Institution of Oceanography, UC San Diego, La Jolla, CA, USA
[3]Swiss Seismological Service (SED), ETH Zürich, Switzerland
[4]Department of Geophysical Engineering, Institut Teknologi Sepuluh Nopember, Indonesia
[5]GFZ, Helmholtz Centre, Potsdam, Germany

Key Points:

- We use 3D dynamic rupture models to analyse how fault properties affect long-period velocity pulse variability.
- Our set of 3D dynamic rupture models is capable of reproducing pulse amplitude variability well.
- Off-fault fracture networks add additional variability to near-fault pulse orientations.

Corresponding author: Rachel Preca Trapani, R.Preca@lmu.de

Abstract

Capturing ground motion variability, especially in near-fault long-period velocity pulses, is a key challenge for seismic hazard assessment. Empirical methods often rely on simplified assumptions and may not fully capture the non-linear interplay of source, path, and site effects. Physics-based dynamic rupture simulations offer a self-consistent alternative, but their ability to reproduce variability in near-fault ground motions, such as velocity pulse orientation, period, and amplitude, remains uncertain. We systematically investigate the effect of fault geometry and on-fault heterogeneities in a suite of 3D dynamic rupture simulations of the 2023 Kahramanmaraş, Türkiye, earthquake. We compare dynamic rupture scenarios that separately incorporate large-scale fault waviness, fractal fault roughness, heterogeneous critical slip-weakening distance, heterogeneous dynamic friction, and supershear versus subshear initiation, each resolving up to at least ~ 1 Hz. We systematically analyse the influence on rupture dynamics, frequency content, and long-period pulse variability, while ensuring all models have comparable seismic moment rate release. While all models capture near-fault pulse amplitude variability, supershear initiation and fracture energy heterogeneity exert the strongest influence on pulse period and orientation. Despite added complexity, most modelled pulses remain predominantly fault-normal, contrasting observed broader ranges of orientations, but supershear rupture speed locally increases variability in pulse orientation. We discuss a simpler main fault model incorporating >700 off-fault fractures, which increases variability in both pulse amplitude and orientation, highlighting the importance of fault zone complexity. Incorporating both heterogeneous on-fault frictional properties and off-fault complexity is promising for advancing realistic, non-ergodic ground motion models and physics-based seismic hazard assessment.

Plain Language Summary

Earthquake shaking can vary a lot depending on how the fault moves, the path seismic waves take, and local ground conditions. Traditional models often simplify these factors and struggle to capture the full range of shaking patterns. In this study, we use advanced 3D computer simulations to examine the 2023 Kahramanmaraş earthquake. We look at how features, such as fault shape, multi-scale roughness, variations in fault friction, and the speed at which the rupture starts, affect the resulting ground motion. We find that while the overall energy release and frequency content of the shaking are relatively stable, certain factors, such as very fast rupture speeds and variations in the fault's resistance to slipping, strongly influence the size, duration, and direction of a specific type of ground shaking known as a long-period velocity pulse. Despite these complexities, the strongest shaking tends to remain aligned roughly perpendicular to the fault. We also consider a model with a network of fractures around the fault, which shows increased variability in pulse amplitude and direction. These findings therefore improve our understanding of how earthquake shaking varies, which is important for better predicting earthquake impacts and improving hazard assessments.

1 Introduction

Ground motion variability stems from the non-linear combination of source, path and site effects, which can be difficult to capture through empirical ground motion models (GMMs) (Bommer et al., 2004) as they often rely on simplified representations and limited near-fault data (Strasser et al., 2009; Somerville et al., 1997; Lin et al., 2011; Bray & Rodriguez-Marek, 2004). Data-constrained 3D dynamic rupture simulations can help address this challenge by simulating realistic, non-ergodic ground motions in a self-consistent way (Aochi & Madariaga, 2003; Harris & Abrahamson, 2014; Wollherr et al., 2019; Hu et al., 2022; Yao & Yang, 2023; Gallovič & Ľ. Valentová, 2023), while reproducing a variety of geodetic, seismic and tsunami data (e.g., Taufiqurrahman et al., 2022; Tinti et al., 2021).

Velocity pulses are long-period and large-amplitude near-fault ground motions, which tend to be highly variable within a 20 km distance from the fault (Withers, Olsen, Day, & Shi, 2019; Baltzopoulos et al., 2023; M.-H. Yen et al., 2025). Such velocity pulses have been shown to correlate with substantial damage but are challenging to account for in seismic hazard assessment (e.g., Heaton et al., 1995; Strasser & Bommer, 2009; Chioccarelli & Iervolino, 2010; F. Wu et al., 2023; Ertruncay & Costa, 2024). They are mainly due to two distinct source effects (Türker et al., 2023): (i) rupture direction relative to the site, i.e. forward or backward directivity, and (ii) permanent ground displacements such as fling-step effects. They represent the cumulative rupture effect concentrated into a single, high-energy arrival and, contrary to earlier assumptions, occur in multiple orientations beyond the fault-normal direction (Shahi & Baker, 2014; Chang et al., 2025).

Directivity pulses occur when the rupture propagates towards (or away from) a recording site. They are typically observed as two-sided, large-amplitude pulses in recorded near-fault velocity waveforms. In contrast, fling-step pulses are characterised by a one-sided large-amplitude velocity pulse. In practice, pulse shapes are more complex and can include ambiguous or multiple-sided forms, occurring at a range of orientations (Chang et al., 2025). Site effects, such as resonance effects, can amplify pulse-like signals, and heterogeneities in fault properties and geometric complexities during dynamic rupture may add variability to their characteristics (Ertruncay & Costa, 2024; M.-H. Yen et al., 2025).

The 2023 Kahramanmaraş Türkiye earthquake sequence was devastating, causing widespread severe damage and tens of thousands of fatalities (Reitman, Briggs, Barnhart, Hatem, et al., 2023). It comprised a doublet of large earthquakes, the M_w 7.8 Pazarcık and the M_w 7.6 Elbistan events. The Pazarcık earthquake was a left-lateral strike-slip rupture that nucleated on the Nurdağı-Pazarcık splay Fault (NPF) at $\sim$ 10 km depth, before branching onto the East Anatolian Fault (EAF) and rupturing a total length of $\sim$350 km (Figure 1a, Jia et al. (2023); Melgar et al. (2023); Delouis et al. (2024)). About 9 hours later, the Elbistan earthquake, also a left-lateral strike-slip event, nucleated 90 km north of the EAF at 7 km depth and ruptured $\sim$ 170 km of the Sürgü-Çardak Fault (SCF) (Mai et al., 2023; Barbot et al., 2023; Chang et al., 2025). The dynamics of the rupture sequence were complex, with supershear propagation on multiple fault segments (Abdelmeguid et al., 2023; Ren et al., 2024; Gabriel et al., 2023; Rosakis et al., 2025).

The earthquake doublet struck densely populated regions, causing structural damage, including failure of some recently constructed buildings (Ertruncay & Costa, 2024). Several studies suggest that near-fault velocity pulses may have contributed to this damage, although their role and prevalence remain debated. Observed ground motions in parts of the affected region exceeded the demands anticipated by building codes, particularly at longer periods where empirical models tend to underestimate response spectra (Baker, 2007; Ozkula et al., 2023; Akinci et al., 2025). It was a complex rupture sequence that potentially reached supershear rupture speeds at different fault segments (Abdelmeguid et al., 2023; Ren et al., 2024; Delouis et al., 2024; Rosakis et al., 2025). Supershear rupture speeds have been suggested to be responsible for the plenitude of impulsive motion (Ertruncay & Costa, 2024), as have other source mechanisms and near-fault complexities (Graves & Pitarka, 2016; Withers, Olsen, Day, & Shi, 2019; Lozos et al., 2025).

A recent analysis by M.-H. Yen et al. (2025) highlights the lack of pulse property variability captured in dynamic rupture models of the 2023 Kahramanmaraş earthquake (Figure 1b, (Jia et al., 2023)). Recent near-fault strong-motion analysis by B. Wu et al. (2025) of the M_w 7.8 Kahramanmaraş earthquake shows a loss of horizontal polarity and reduced between-component coherence, implicating small-scale source and near-fault structural processes not captured by dynamic rupture models either. This motivates this study focusing on the physical controls of velocity pulses and high-frequency radiation, aiming to advance realistic, non-ergodic ground motion models and physics-based seismic hazard assessment.

2 Methods

2.1 Velocity Pulse Analysis

We analyse near-fault, long-period velocity pulses following Shahi and Baker (2014). Their wavelet-based algorithm searches for pulse-like motion in two horizontal, orthogonal ground motion components. This algorithm identifies ground motions in any orientation most likely to contain directivity pulses by performing a two-component wavelet transform to produce coefficients for every orientation. The corresponding wavelet coefficients are used to extract up to five candidate pulses from the velocity time histories at a given station. The algorithm then classifies the candidate pulses as "pulse-like" or "non-pulse-like" according to the defined threshold, which is related to the peak ground velocity (PGV) of the record. This method is capable of classifying observed and modelled near-fault ground motion through a quantitative and reproducible classification. Applying this method to the near-field synthetics of our dynamic rupture models allows us to account for potential pulses in any orientation, consistent with observational evidence that pulse-like motion is not only confined to the fault-normal direction (Somerville et al., 1997).

In more detail, the discrete wavelet transform is applied to the two horizontal components of the ground motion time histories to obtain wavelet coefficients. These coefficients are formed by representing the signal as a sum of scaled and translated Daubechies mother wavelets (Daubechies, 1993) in the time-frequency domain. This decomposition reveals how strongly each wavelet matches the signal at different times and scales, thereby indicating which frequencies dominate at which points in the record. This means that large coefficients indicate concentrated energy in a narrow time-frequency region, which is characteristic of a strong pulse. Using the coefficients of the two orthogonal components, the maximum wavelet amplitude is efficiently computed across all orientations. The orientation at which this maximum occurs is interpreted as the direction most likely to contain a pulse. The two horizontal components are then rotated into this orientation. The rotated single signal is referred to as the "original signal", following (Shahi & Baker, 2014; M.-H. Yen et al., 2025). From the original signal, a candidate pulse is extracted (see Figure S1) to obtain its properties, such as pulse amplitude, period (T_p), and orientation. This procedure is repeated on the original signal without the extracted pulse signal to identify up to five non-overlapping candidate pulses, ensuring that potential pulses at different times or frequencies are also captured.

The "pulse criterion" defined by Shahi and Baker (2014) is then calculated for each identified candidate pulse using a nonlinear Support Vector Machine (SVM)–based pulse indicator, combined with an early-arrival criterion to remove late-arriving pulses. This pulse criterion ranks each candidate pulse. Only the one top-ranked pulse-like identified candidate is retained. Pulse classification is based on the pulse indicator (PI), which combines (i) the energy ratio of the residual to the original signal (ER), (ii) the PGV ratio of the residual and original signals ($\mathrm{PGV}_{\mathrm{ratio}}$), and (iii) the PGV of the original signal (PGV). First, a principal component (PC) of ER and $\mathrm{PGV}_{\mathrm{ratio}}$ is formed:

$$\mathrm{PC} = 0.63\,\mathrm{PGV}_{\mathrm{ratio}} + 0.777\,\mathrm{ER}\,. \tag{1}$$

Then the pulse indicator is

$$\mathrm{PI} = 9.384(0.76 - \mathrm{PC} - 0.616\,\mathrm{PGV})(\mathrm{PC} + 6.914 \times 10^{-4}\,\mathrm{PGV} - 1.072) - 6.179\,. \tag{2}$$

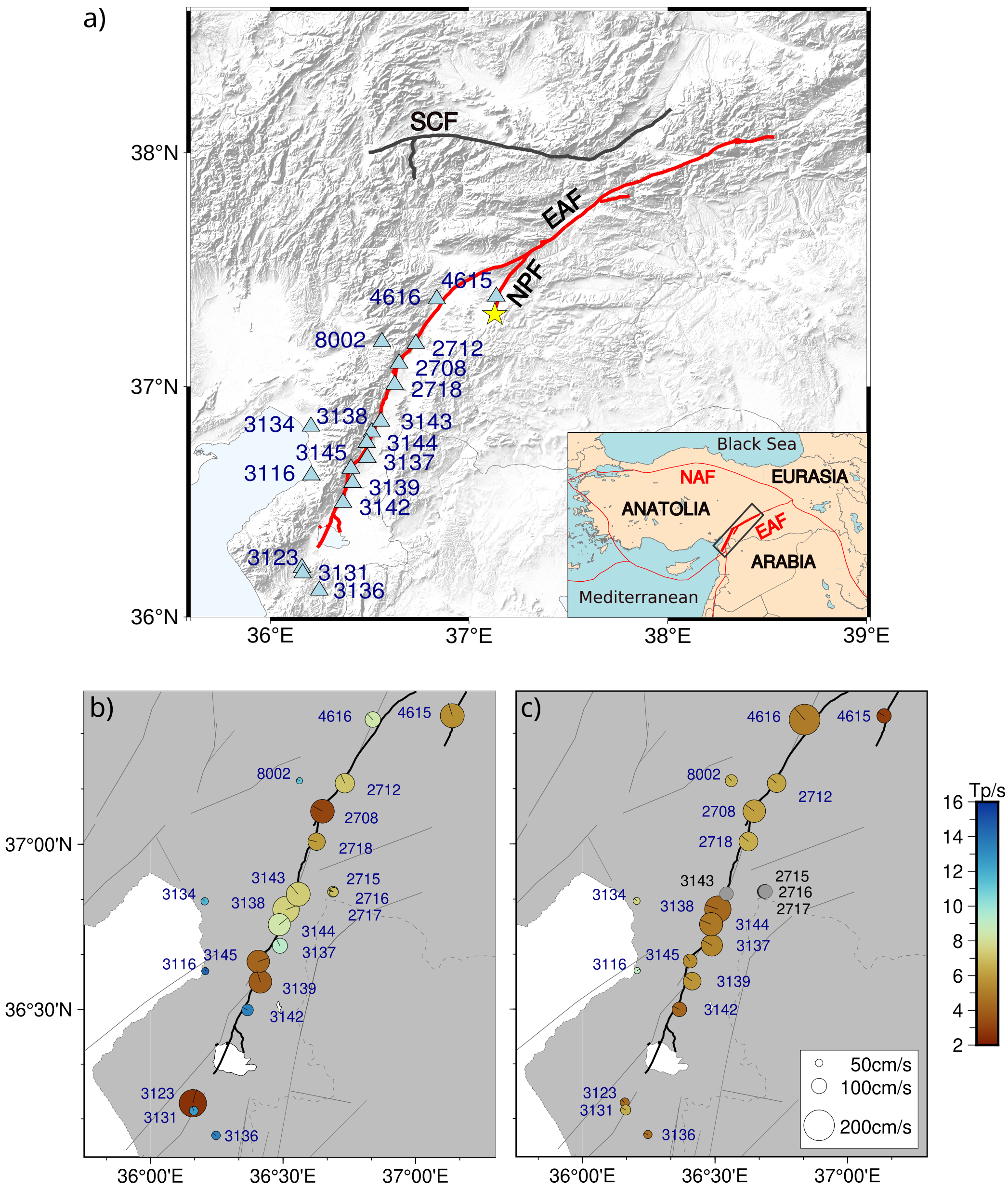

Figure 1: a) The study area highlighting the 2023 M_w 7.8 Kahramanmaraş earthquake surface rupture (red lines, (Reitman, Briggs, Barnhart, Jobe, et al., 2023)). The earthquake initiated on the Nurdağı-Pazarcık splay Fault (NPF) and continued onto the East Anatolian Fault (EAF) in a bilateral manner. For completeness, the grey lines show the surface rupture of the 2023 Mw 7.7 Elbistan earthquake that broke the Sürgü–Çardak Fault (SCF, (Reitman, Briggs, Barnhart, Jobe, et al., 2023)). The yellow star depicts the AFAD epicentre, and the blue triangles represent the AFAD near-fault stations (see Open Research Section) used in this study. The inset shows the regional tectonics and major plate boundary faults (red lines), including the North Anatolian Fault (NAF) and EAF. The rectangle highlights the study area. b) Reproduction of M.-H. Yen et al. (2025)'s results showing long-period near-fault pulse properties extracted from observational data (ESM, Luzi et al. (2020)) and c) from the dynamic rupture model of (Jia et al., 2023) for the 2023 Kahramanmaraş earthquake. The circle size corresponds to the pulse amplitude, the colour corresponds to the pulse period (T_p), and the lines within the circles represent the pulse orientation. Black lines show the surface rupture trace (Reitman, Briggs, Barnhart, Jobe, et al., 2023), grey lines show the mapped active faults (Styron & Pagani, 2020), and dashed lines show the boundary between Türkiye and Syria. See also Figure S2.

This formulation creates a curved decision boundary in the feature space, replacing Baker's (2007) linear-regression boundary and avoiding the need for an imposed PGV threshold. A ground motion is labelled as pulse-like when PI $>$ 0 and non-pulse-like when PI < 0. The principal component formulation ensures that PC captures the dominant variance shared between the energy and PGV ratios, making the classifier more robust and reducing dimensionality. To focus on directivity pulses, which typically arrive early in the time history, we apply an additional timing criterion based on the cumulative square velocity (CSV), defined as:

$$\mathrm{CSV}(t) = \int_0^t V^2(u)du\,. \tag{3}$$

Where $V(u)$ is the velocity of the signal at time u. Through this, we search for the time at which CSV(t) is at x% of the total CSV of the signal. This is represented as $t_{x\%,\mathrm{orig}}$ and $t_{x\%,\mathrm{pulse}}$ for the original signal and the extracted pulse, respectively. A pulse is rejected if it occurs too late, specifically when $t_{17\%,\mathrm{orig}} \leq t_{5\%,\mathrm{pulse}}$. Only pulses that pass both the pulse indicator criterion and the timing requirement are considered directivity pulses.

2.2 3D Dynamic Rupture Model Setup

We focus on dynamic rupture models of the M_w 7.8 Kahramanmaraş earthquake, the first event of the 2023 Türkiye doublet. Our 3D dynamic rupture models are based on the setup presented in Gabriel et al. (2023), hereafter referred to as the "reference model" (Model 1), which has been validated with seismic, geodetic and optical observations. In contrast to the dynamic rupture models in Jia et al. (2023), no smaller-scale initial prestress or fault strength heterogeneity is prescribed in our reference model. Dynamic rupture models require the definition of a set of initial conditions (e.g., Ramos et al., 2022) which govern the rupture, including the fault strength, initial stress orientation and magnitude, the fault geometry, and off-fault material properties. The initial conditions of the reference model are summarised in Section 2.3 (see also Table 1).

In this study, we analyse a set of five 3D dynamic rupture models, each differing from the reference model (Model 1) by one added source of physical or geometrical complexity (Figure 2). These variants will be referred to as: Model 2 ("supershear initiation model"): supershear rupture speed initiation, from Gabriel et al. (2023); Model 3 ("roughness model"): multi-scale on-fault roughness; Model 4 ("D_c model"): heterogeneous distribution of critical slip-weakening distance (D_c); Model 5 ("μ_d model"): heterogeneous distribution of dynamic friction coefficient (μ_d); and Model 6 ("waviness model"): large-scale fault waviness. Our model modifications are motivated by the need to understand what drives the generation and variability of long-period velocity pulses (e.g., M. Yen et al., 2021; Türker et al., 2023; M.-H. Yen et al., 2025) and whether such heterogeneities influence the high-frequency content of near-fault ground motions (e.g., Vallée et al., 2008; Shi & Day, 2013; B. Wu et al., 2025).

In all six models considered in this study, rupture is initiated on the NPF at the AFAD hypocentral location (37.043°N, 37.288°E) and then ruptures across the EAF (Figure 1a). All models share the same numerical setup, including the computational mesh and nucleation procedure. Exceptions include the larger meshes required by Models 3 and 6 (Section 3.2) and minor adjustments to the prestress ratio and initial stress in Models 3, 5, and 6 to ensure comparable dynamic rupture propagation across the fault system (Section 2.3).

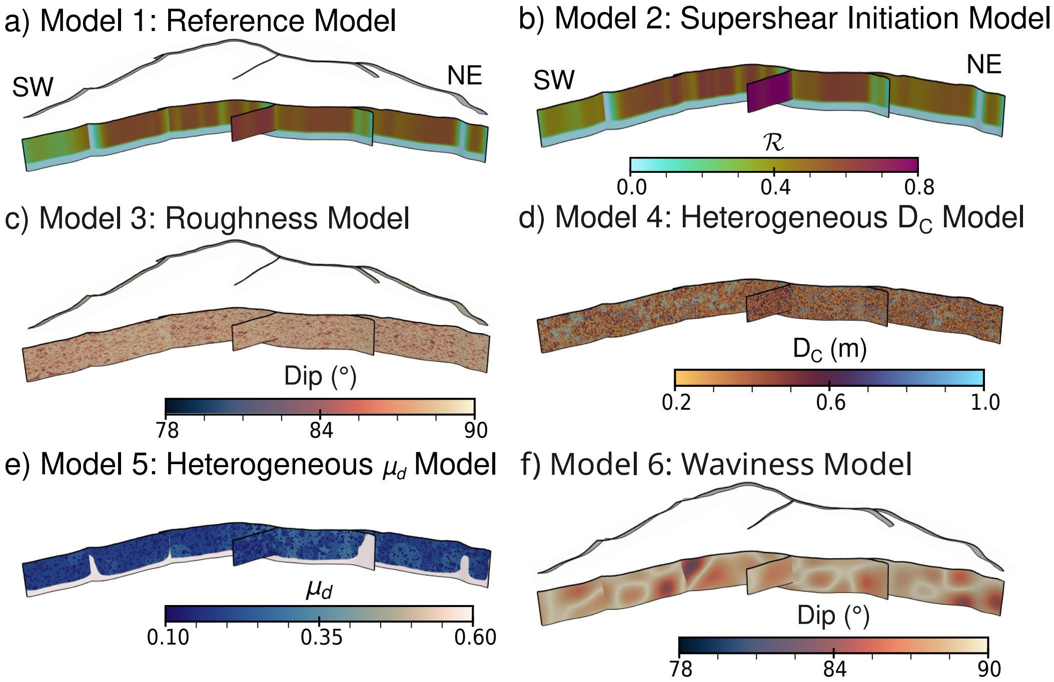

Figure 2: Overview of the reference and five new dynamic rupture models of the 2023 M_w 7.8 Kahramanmaraş earthquake analysed in this study. a) Model 1: the reference model by Gabriel et al. (2023); b) Model 2: supershear initiation c) Model 3: multi-scale fault roughness d) Model 4: heterogeneous D_c e) Model 5: heterogeneous μ_d f) Model 6: large-scale fault waviness.

2.3 Fault Strength, Friction and Initial Stress

In all simulations, fault strength, τ, is governed by a linear slip-weakening friction law (Ida, 1972; Palmer et al., 1973; D. J. Andrews, 1976; Day, 1982). A fault begins to slip when the shear stress locally exceeds the peak fault strength τ_p. The fault strength then decreases linearly from a static peak value, τ_p, to a dynamic level, τ_r, over a critical slip-weakening distance, D_c, as:

$$\tau = \begin{cases} \tau_p - (\tau_p - \tau_r)\frac{u}{D_c}, & u < D_c\,, \\ \tau_r, & u \geq D_c\,. \end{cases} \tag{4}$$

where $\tau_p = c + \mu_s \sigma'_n$, $\tau_r = \mu_d \sigma'_n$. μ_s is the static coefficient of friction, μ_d is the dynamic coefficient of friction, u is the accumulated fault slip, and σ'_n is the effective normal stress accounting for pore fluid pressure P_f. Fault strength is defined as

$$\tau = c + \mu \sigma'_n\,. \tag{5}$$

where c is the frictional on-fault cohesion, the part of fault strength that does not depend on effective normal stress.

In the reference model, the static coefficient of friction is set to $\mu_s = 0.6$, the dynamic coefficient of friction to $\mu_d = 0.2$ and the critical slip-weakening distance to D_c = 0.5 m (see Table 1). We set the on-fault frictional cohesion c to 0.5 MPa below 6 km depth and increase it linearly up to 1.5 MPa at a depth of 0 km to prevent unrealistically low shallow fault strength (Gabriel et al., 2023).

In all models, we expose the fault system to an Andersonian stress regime representing strike-slip faulting, i.e. the intermediate compressive stress σ_2 is vertical, (Anderson, 1905, 1951). As in Gabriel et al. (2023), the orientation of the maximum horizontal compressive stress, SH_{max}, is variable and constrained by a regional stress tensor inversion from focal mechanisms (Güvercin et al., 2022) (Figure S3a). The magnitudes of the principal stresses σ_1, σ_2, and σ_3 (with $\sigma_1 > \sigma_2 > \sigma_3$) are controlled by the relative prestress level $\mathcal{R}_0$ of a (virtual) optimally oriented fault, the effective lithostatic stress σ'_{zz} and the stress shape ratio ν (Ulrich et al., 2019).

Up to 6 km depth, the effective lithostatic stress σ'_{zz} increases linearly with depth and is equal to the lithostatic stress σ_{zz} reduced by the effect of the pore fluid pressure P_f. P_f is assumed proportional to the lithostatic stress, $P_f = \gamma \sigma_{zz}$, with γ the fluid-pressure ratio (Ulrich et al., 2019):

$$\sigma_{zz}(z) = \rho\, g\, z\,. \tag{6}$$

$$\sigma'_{zz}(z) = (1-\gamma)\,\sigma_{zz}\,. \tag{7}$$

where $\rho = 2670$ kg m^{-3} is the overburden rock density, g is the acceleration gravity, and z is the depth. We assume an over-pressured pore fluid state with γ=0.66. Below 6 km depth, the pore fluid pressure gradient mirrors the lithostatic stress gradient, leading to constant effective lithostatic stress of 52 MPa (Rice, 1992; Suppe, 2014; Madden et al., 2022).

From the orientation and magnitude of the three principal stress components, the full 3D initial stress tensor is computed. The shear and normal stresses acting on the non-planar fault surfaces are then obtained by projecting the resulting tensor onto the non-planar fault segments, naturally producing spatial variations in τ_0 and σ_n.

Local fault strength and dynamic stress drop are governed by the relative prestress ratio, $\mathcal{R}$ (Aochi & Madariaga, 2003; Ulrich et al., 2019), which varies across the fault system (Figure S4). $\mathcal{R}$ represents the fault-local ratio of the maximum potential stress drop over the frictional breakdown strength drop, as:

$$\mathcal{R} = \frac{\tau - \mu_d \sigma'_n}{(\mu_s - \mu_d)\sigma'_n} . \tag{8}$$

When $\mathcal{R}$=1, the fault is critically stressed and optimally oriented. The $\mathcal{R}$ ratio is related to the seismic S ratio (Das & Aki, 1977) as $S = 1/\mathcal{R} - 1$. We prescribe $\mathcal{R}_0$, the maximum value of $\mathcal{R}$ of an optimally orientated fault segment in a given stress regime. The fault local $\mathcal{R} \leq \mathcal{R}_0$ varies with fault geometry, initial stresses and frictional heterogeneities (Figure S4). In the reference model, $\mathcal{R}_0 = 0.62$ across the NPF and varies across the EAF (Figure 3a). Figures 3b-g illustrate the prescribed $\mathcal{R}_0$ in our six dynamic rupture models.

In Model 2, we prescribe the same $\mathcal{R}_0$ as in the reference model except along the NPF, where $\mathcal{R}_0$ increased to initiate at supershear rupture speeds (Section 3.1). Model 4 has identical $\mathcal{R}_0$ and thus $\mathcal{R}$-distribution to the reference model since $\mathcal{R}$ is independent of D_c (Eq. 8). For Models 3, 5 and 6, adopting the same $\mathcal{R}_0$ distribution as used in the reference model prevents dynamic rupture from propagating across the EAF, failing to pass the NPF-EAF junction. We find in trial-and-error simulations (not shown) that achieving comparable rupture dynamics in these Models requires a change in the prescribed $\mathcal{R}_0$. Figure S3b shows the rupture speed fault output for one of these trial-and-error simulations for Model 6, in which $\mathcal{R}_0$ is prescribed too large along the eastern portion of the EAF, resulting in supershear rupture speeds in this section. For Models 3 and 5, we additionally prescribe a change in SH_{max} west of the NPF-EAF junction (Supplementary Figure S3a). Varying only $\mathcal{R}_0$ is not sufficient to sustain dynamic rupture across the junction. Compared with the reference model, multi-scale fault roughness (Model 3) and spatial heterogeneity in μ_d (Model 5) add additional shear resistance (Dunham et al., 2011; Fang & Dunham, 2013; Tinti et al., 2021; Taufiqurrahman et al., 2022).

Parameter	Notation	Reference Model
Static friction coefficient	μ_s	0.6
Dynamic friction coefficient	μ_d	0.2
Critical slip weakening distance	D_c [m]	0.5
Maximum cohesion	c [MPa]	1.5

Table 1: Dynamic rupture parameter values for the reference model.

2.4 Fault Geometry and Nucleation

We adopt the same fault geometries as in Gabriel et al. (2023), which are informed from space geodesy and seismicity, including aftershock locations. This fault system geometry consists of five intersecting segments with a dip of 90° for the NPF and the EAF reaching a depth of 20 km that capture large-scale geometrical complexities, such as fault bends, step-overs and secondary segments, across which the earthquake propagated (Figure 1b).

Dynamic rupture simulations require prescribed nucleation in order to initiate spontaneous rupture propagation (e.g., Bizzarri, 2010; Galis et al., 2015). We use a smooth nucleation procedure for all simulations that involves a forced rupture across a prescribed patch of 2 km radius (Gabriel et al., 2012; Harris et al., 2018). At the given nucleation time, the friction coefficient is artificially reduced to its dynamic value. The nucleation then grows smoothly in time as a kinematically driven subshear crack-like rupture with rupture speed $V_r \sim 2400$ m/s (Gabriel et al., 2023). All models prescribe nucleation at the hypocenter location of the Disaster and Emergency Management Authority (AFAD) of Türkiye (see Open Research Section).

2.5 Velocity Model and Off-fault Plasticity

The elastic properties of the medium are constrained by the 1D velocity model of Güvercin et al. (2022). We do not include viscoelastic attenuation. Table S1 details the variation in P-wave c_p and S-wave c_s velocities with depth.

We include non-associative Drucker-Prager off-fault plasticity in all dynamic rupture models (D. Andrews, 2005; Wollherr et al., 2018), without changing its parameterisation between models. The plastic cohesion, C_{plast}, controls how much stress the off-fault medium can withstand before deforming plastically. We follow previous work (e.g., Withers, Olsen, Shi, & Day, 2019; Yeh & Olsen, 2024; Li et al., 2025; Schliwa et al., 2025) and define plastic cohesion to vary with the 1D depth-dependent shear modulus $\mu(z)$, following the plastic cohesion "model 3" described in Roten et al. (2014) for weak rocks, as:

$$C_{plast} = 10^{-4}\mu(z)\,. \tag{9}$$

This description allows for a range of cohesion values between 0 and 10 MPa that are observed in laboratory experiments and are commonly used in dynamic rupture studies in nonlinear media (e.g., D. Andrews, 2005; Dunham et al., 2011), and being depth dependent. At near-surface depths shallower than 2 km, where confinement stresses are low, we taper plastic cohesion to $C_{plast} = 4.85$ MPa as:

$$C_{plast} = 2 \times 10^{-4} \times \max\left(\mu(z),\, 2 \times 10^{10}\right)\,. \tag{10}$$

This tapering is applied to achieve a good match between the measured and modelled surface fault offsets (Gabriel et al., 2023). Models without the tapering (i.e. that assume a lower plastic cohesion value near the surface) underestimate the slip at shallow depths. For numerical reasons (D. Andrews, 2005), the initiation of plastic yielding is governed by viscoplastic relaxation, allowing stress to relax gradually over a constant timescale $T_v = 0.05$ s, independent of spatial discretisation (Wollherr et al., 2018).

We note that off-fault plastic deformation depends on the initial stress state in the volume, which varies slightly between models 2, 4 and 3, 5 and 6. In addition, fault roughness and fault waviness will generate enhanced off-fault plasticity compared to planar fault models (e.g., Dunham et al., 2011). Analysing these differences is beyond the scope of this study, and should be addressed in future work.

2.6 Numerical Method

We use the open-source software package SeisSol (Gabriel et al., 2025) to solve the 3D spontaneous dynamic rupture and seismic wave propagation problem. SeisSol uses the Arbitrary high-order accurate DERivative Discontinuous Galerkin (ADER-DG) finite element method (e.g., Dumbser & Käser, 2006; Pelties et al., 2012). SeisSol combines non-linear on-fault frictional failure and high-order accurate propagation of seismic waves and is optimised for modern high-performance computing infrastructure (e.g., Breuer et al., 2014; Heinecke et al., 2014; Uphoff et al., 2017; Krenz et al., 2021). It has

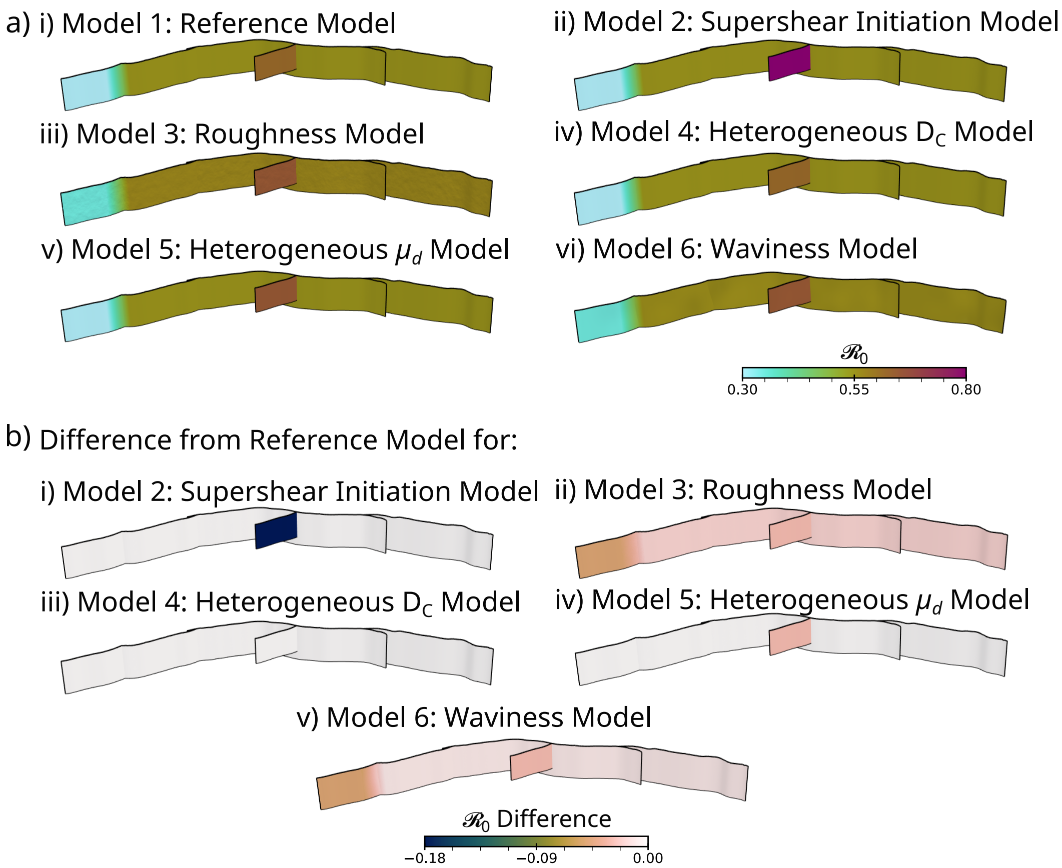

Figure 3: a) $\mathcal{R}_0$ for all six models. b) The difference in $\mathcal{R}_0$ between the reference model and the models with added complexities [Difference = Reference Model - Complexity Model].

been verified through several dynamic rupture benchmark problems (Pelties et al., 2014; Harris et al., 2018; Taufiqurrahman et al., 2022; Vyas et al., 2023).

2.7 Mesh and Resolution

The reference model and models 2, 4, and 5 use the same unstructured tetrahedral mesh, which is constructed of ∼30 million elements. Simulating fault roughness for Models 3 and 6 involves re-meshing the more complex fault geometries whilst maintaining the resolution used in the other models. We generate a larger mesh consisting of ∼ 50 million elements that covers a slightly larger area and adapts to the band-limited self-similar fractal fault surfaces (see Section 3.2, 3.5 and Table S2). The smallest on-fault element edge length is $h = 300$ m in all models. Elements become gradually coarser with distance from the faults. We define a 400 × 200 × 25 km high-resolution area in all models, which encompasses the entire fault system, as well as the local strong ground motion stations. Within this region we resolve seismic wave propagation up to frequencies of at least 1 Hz. The meshes are accounting for topography using high-resolution (450 m) data from the Shuttle Radar Topography Mission (SRTM) Digital Elevation Model (DEM) (Farr et al., 2007).

3 Increasing Complexity in Dynamic Rupture Models of the M_w 7.8 Kahramanmaraş Earthquake

3.1 Model 2: Supershear Initiation

We analyse supershear rupture speed initiation along the NPF, using the alternative model presented in Gabriel et al. (2023). This analysis is motivated by related studies (e.g., Rosakis et al., 2025; Abdelmeguid et al., 2023; Ren et al., 2024) that analyse near-field ground motion records and geodetic data to constrain rupture speed along the NPF.

Supershear rupture propagation has been linked to enhanced high-frequency radiation (e.g., Spudich & Frazer, 1984; Bizzarri & Spudich, 2008) and strong directivity pulses (Ertruncay & Costa, 2024), rendering it an interesting mechanism for explaining the observed variability in long-period velocity pulses. To achieve supershear rupture speed initiation on the splay NPF, as opposed to subshear initiation in the reference model, we increase the maximum relative stress ratio ($\mathcal{R}_0$) from $\mathcal{R}_0$=0.62 to 0.8 in Model 2. The modified $\mathcal{R}_0$ distribution is shown in Figure 3a.ii and b.i

3.2 Model 3: Multi-Scale Fault Roughness

In Model 3, we introduce multi-scale fault roughness motivated by previous work illustrating the impact of fault roughness on high-frequency radiation (Shi & Day, 2013; Withers, Olsen, Day, & Shi, 2019; Taufiqurrahman et al., 2022). However, the effect of fault roughness on long-period, near-fault velocity pulses remains unexplored. Fault roughness encompasses the natural variety of geometrical deviations from planarity at different scales along the fault surface. To represent natural fault roughness (W. Power et al., 1987; Renard et al., 2006), we change the originally planar fault surfaces of the NPF and EAF to band-limited, self-similar fractal surfaces (Candela et al., 2009, 2012), while preserving sufficient mesh resolution (see Section 2.7).

Fault roughness can be represented through a fractal fault surface topography (W. Power et al., 1987), described by two parameters. First, the Hurst exponent, which may range between $0 \leq H < 1$, as $H = 1$. This means roughness is self-similar such that it remains statistically invariant at different scales. Second, the amplitude-to-wavelength ratio, α, describes the amplitude of fault roughness and how it varies with wavelength:

$$\alpha = h_{\mathrm{rms}}/L\,, \tag{11}$$

where L is the total along-strike length of the fault and h_{rms} represents the root mean square (rms) roughness of a 2D profile of the fault surface (Dunham et al., 2011; Shi & Day, 2013; Fang & Dunham, 2013). Here, the amplitude-to-wavelength ratio is set to $\alpha = 10^{-2.3}$, consistent with observed roughness of natural faults (W. L. Power & Tullis, 1991). We impose fractal roughness that is band-limited between λ_{min} and λ_{max}. λ_{min} =300 m, corresponding to the smallest on-fault element size, and λ_{max} =10 km (Figure 2c). Compared to the fault system size, the imposed fault roughness remains relatively small-scale, preserving the large-scale reference fault geometries. Figure 2c also illustrates variations of up to $-12°$ in dip angle about the reference value of 90° due to the added roughness.

To sustain rupture across the entire EAF, we slightly adjust the prescribed $\mathcal{R}_0$ and maximum horizontal stress orientation (SHmax), based on trial-and-error dynamic rupture simulations (not shown). We increase $\mathcal{R}_0$ from 0.62 to 0.65 along the NPF, from 0.55 to 0.57 along most of the EAF, and from 0.3 to 0.35 on the westernmost EAF segment (Figure 3b.ii). We slightly rotate SH_{max} locally (Supplementary Figure S3a) from $-10°$ to $-8°$ at point iii and from 15° to 17° at point iv to overcome the additional shear resistance due to the 3D "roughness drag" (Fang & Dunham, 2013; Taufiqurrahman et al., 2022). These changes fall within observational uncertainties of the regional stress field (Heidbach et al., 2010).

3.3 Model 4: Heterogeneous D_c

Previous work shows that the acceleration or deceleration phases of a dynamic rupture generate high-frequency content (Madariaga, 1977; Vallée et al., 2008; Li et al., 2022). We introduce a variable critical slip-weakening distance (D_c) value across the fault in an attempt to generate this "stop-and-go" effect of the rupture propagation. We apply this to explore the effects on high-frequency content by generating variable fracture energy by prescribing patches of variable D_c, as well as to explore whether these changes affect directivity pulse characteristics.

In order to simulate variable D_c, following the approach by Ide and Aochi (2005), we define a fractal distribution of frictional asperities with size-dependent D_c, in turn, defining heterogeneous fracture energy along the EAF. This approach defines families of different patch sizes corresponding to different D_c values that are stacked on each other in a hierarchical manner.

There are a total of 8 families with a fractal dimension of $D = 1.49$, where the smallest patches, that are the most abundant, correspond to D_c values of 0.2 m and a patch radius of 300 m, allowing for patches of faster weakening and more easily propagating rupture fronts. On the other hand, the largest patches have a patch radius of 38,400 m, corresponding to D_c values of 0.9 m and are the least abundant, with only two of the largest patches defined (Figure 2d). These allow for higher fracture energy patches that slow down the rupture front, therefore creating a variable stop-and-go effect on the rupture propagation. Along with a background value of 1 m, the relationship between the number of patches ranging between 0.2 and 0.9 m is varied to produce an overall average D_c value of 0.5 m, as defined in the reference model for the faulting system of the first event.

3.4 Model 5: Heterogeneous μ_d

Fault stresses and strengths are difficult to constrain from observations and therefore tend to be described as constant or varying linearly with depth (e.g., Galvez et al., 2014; Gabriel et al., 2023; Marchandon et al., 2025). Since frictional fault strength is known to impact the rupture propagation (Harris et al., 2018; Tinti et al., 2021), we incorporate a heterogeneous distribution of the dynamic coefficient of friction, μ_d; an often overlooked approach, to explore its effects on rupture propagation speed, and therefore frequency radiation. We implement this through a similar approach as in Model 4, using the Ide and Aochi (2005) approach.

We define fractally distributed frictional asperities with size-dependent values for μ_d, with μ_d values ranging from 0.1 in the smallest and most abundant patches, to 0.3 in the largest and least abundant patches. If μ_d is chosen too large it becomes close to the static friction value and inhibits dynamic rupture. The background value is set to 0.2 to average to an overall distribution of $\mu_d = 0.2$ as in the reference model (Figure 2e). This setup has a total of 7 families with a fractal dimension $D = 1.7$. The smallest patches are of radius $r_0 = 300$ m and the largest patches of radius $r = 19,200$ m. Similar to Model 3, the prescribed $\mathcal{R}_0$ value for the NPF is changed from 0.62 to 0.65 (Figure 3b.iv) and the SH_{max} value for points iii and iv in Figure S3a are changed to $-6°$ and $19°$, respectively.

3.5 Model 6: Large-Scale Fault Waviness

Given that directivity pulses are of low frequencies, we next include geometric complexity that is aimed at low-frequency wavefield generation. For example, Withers, Olsen, Day, and Shi (2019) show that directivity exists prominently at low frequencies for large magnitude earthquakes. We include fault geometry variability, i.e., large-scale fault waviness, comparable to the range in which the long-period pulses are observed. We add large-scale fault waviness through a similar approach as for the fault roughness (Model 3) by prescribing a band-limited self-similar fractal deviation of planarity of the fault surfaces, but now ranging between larger $\lambda_{min} = 20$ km and $\lambda_{max} = 60$ km, and an amplitude-to-wavelength ratio of $\alpha = 10^{-2.5}$. λ_{min} and λ_{max} are chosen specifically to align with periods between 5 - 16 s. Assuming a characteristic wave speed of 2-4 km/s, this results in wavelengths ranging between 10 - 64 km.

The top figure in Figure 2f shows the map view of the fault geometry, highlighting the added waviness, particularly to the west of the NPF–EAF junction, without altering the overall fault geometry. As in c), the bottom figure depicts dip angle variation due to the applied large-scale waviness. As described in Figure 3b.v, the $\mathcal{R}_0$ value along the NPF is set to 0.65, the majority of the EAF is increased to a value of 0.56, while the westernmost segment is increased to 0.35.

4 Results

4.1 Effects on Rupture Dynamics

Model	M_0	M_w
Reference	7.778e+20	7.857
Supershear Initiation	7.962e+20	7.864
Small-Scale Roughness	7.053e+20	7.829
Heterogeneous D_c	7.827e+20	7.859
Heterogeneous μ_d	6.964e+20	7.825
Large-Scale Waviness	7.925e+20	7.863

Table 2: Seismic moment and moment magnitude for all models.

All five new dynamic rupture scenarios of the M_w 7.8 Kahramanmaraş earthquake show overall similar characteristics in rupture dynamics to the reference model and observations (Gabriel et al., 2023; Melgar et al., 2023). Figures 4 to 7 and Table 2, as well as Movies S1 and S2 in the supplementary material, summarise each model's rupture dynamics, discussed in detail in the following.

The total seismic moment magnitude and the moment rate release of all six models is comparable, despite the varying model complexities (Table 2, Figure 4). We see almost identical propagation of slip rate when comparing all models in Movie S1. For all models, the moment rate release between 0 - 12 s represents the rupture along the NPF and a slight decrease in moment rate release at 12 s aligns with the rupture crossing the NPF-EAF junction and continuing at subshear rupture speed. This is followed by an increase in moment rate release at around 20 s, when the rupture also begins to propagate along the western part of the EAF. The moment rate release begins to decrease at around 55 s, when the rupture reaches the end of the eastern part of the EAF, and a final peak can be seen between 60 - 77 s, where the rupture propagates along the final segment of the western part of the EAF. The supershear initiation model (Model 2) stands out with a higher moment rate release at the start of the rupture between 0 and

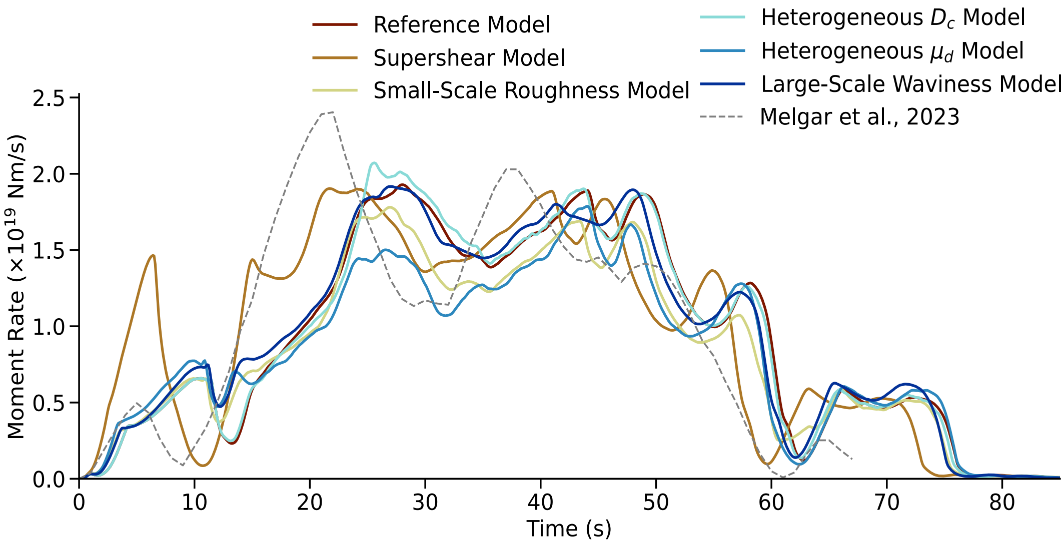

Figure 4: Moment rate release of all six dynamic rupture models along with the moment rate release from the kinematic model of Melgar et al. (2023).

10 s, representing the supershear rupture along the NPF. This allows it to cross the junction earlier than in the other models, with more energy, while following the same moment rate release pattern after the junction.

The heterogeneous D_c model shows slightly higher energy release ($\sim 0.2 \times 10^{19}$ Nm/s) as it traverses the first segment of the eastern part of the EAF compared to the reference model. In contrast, the multi-scale roughness and the heterogeneous μ_d models have a slightly lower seismic moment release ($\sim 0.2-0.5\times10^{19}$ Nm/s) for the majority of the propagation along the eastern part of the EAF and the start of the western part, and have a slightly lower seismic moment compared to the other dynamic rupture models (Table 2).

As shown in Figure 5, all models exhibit similar accumulated fault slip (ASl) distributions. The roughness and μ_d models exhibit up to $\sim$ 5 m less total slip, particularly along the western part of the EAF, compared to the reference model (Figure 5b.ii and iv). The supershear initiation model (Model 2) exhibits higher total slip along the NPF of up to $\sim$ 5 m (Figure 5b.i). We also observe an increase of $\sim$ 1.5 m for the μ_d model (Model 5) along the NPF (Figure 5b.iv).

Figure 6 compares the peak slip rate (PSR) of all models. Geometric and frictional complexities in fault roughness, D_c, and μ_d models lead to a more variable peak slip rate. The D_c asperities only appear to impact the PSR on certain fault segments, such as the entire segment west of the EAF-NPF junction, and the small segment of the EAF. Similarly, PSR increases drastically along the NPF by $\sim$ 6 - 7 m/s for the supershear initiation model (Figure 6b.i). Larger PSR values are also seen in the waviness model compared to the reference model (Figure 6b.v).

Interestingly, the impacts of the asperities in the roughness, D_c, and μ_d models are evident in Figure 6. The PSR increases and decreases along the included asperities, particularly in the μ_d model, where the PSR variability pattern appears to follow the pattern of the defined variable μ_d (Figure 2f).

The rupture speed distributions shown in Figure 7 and Movie S2 also demonstrate similarities in rupture dynamics across models. A smooth and relatively constant, sub-

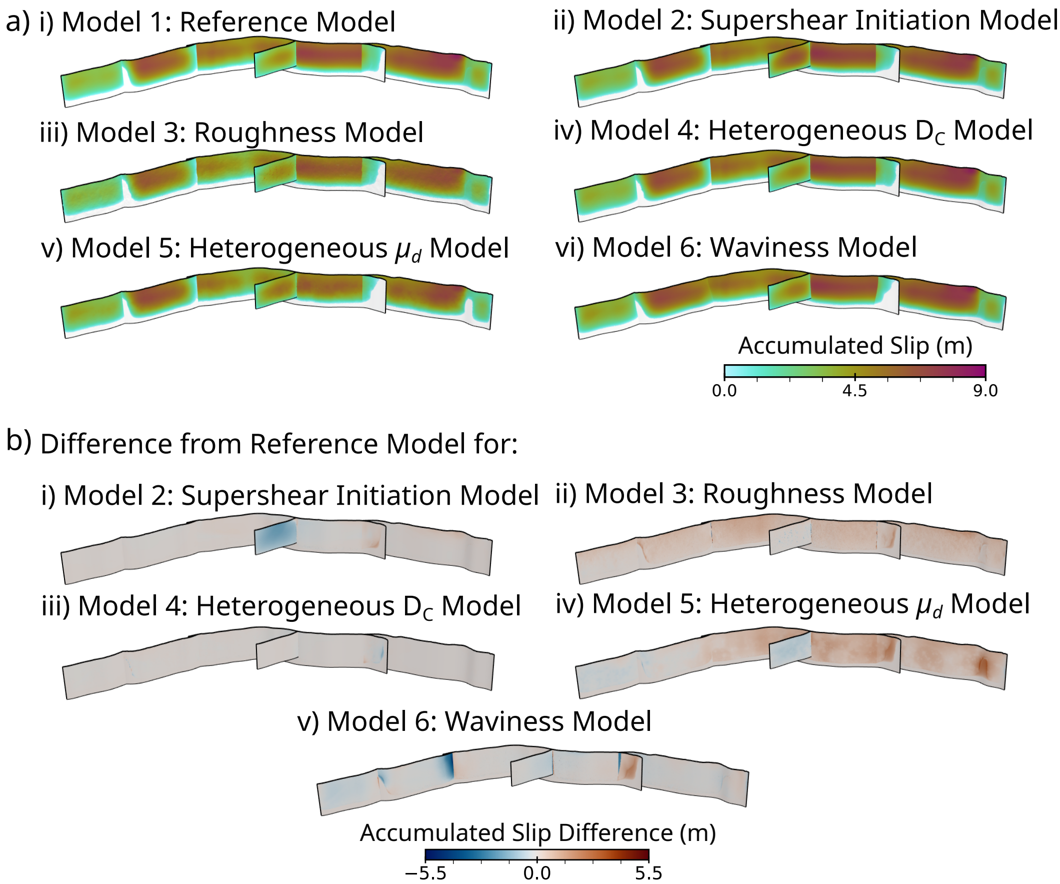

Figure 5: a) Accumulated slip for all six models. b) The difference in the accumulated slip between the reference model and the models with added complexities [Difference = Reference Model - Complexity Model].

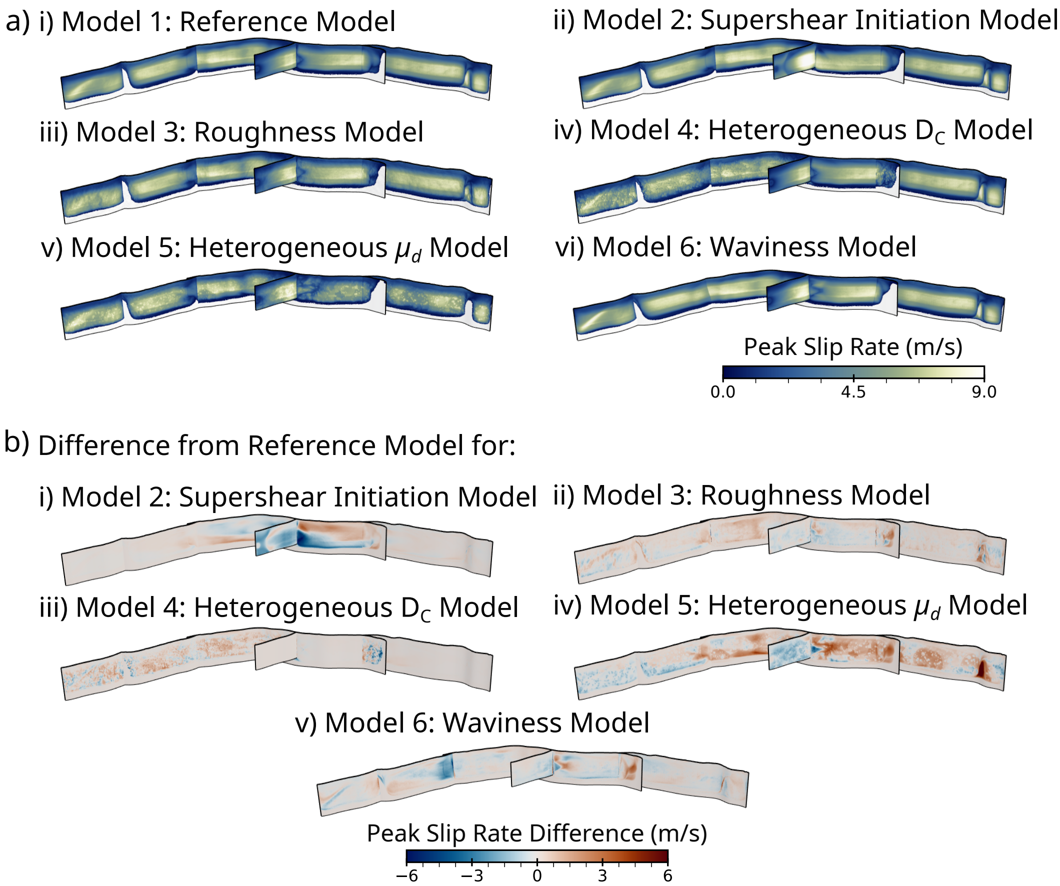

Figure 6: a) Peak slip rate for all six models. b) The difference in peak slip rate between the reference model and the models with added complexities [Difference = Reference Model - Complexity Model]. The values range between -7.3 and 9.1 m/s but are saturated between -6 and 6 m/s for better representation of the differences.

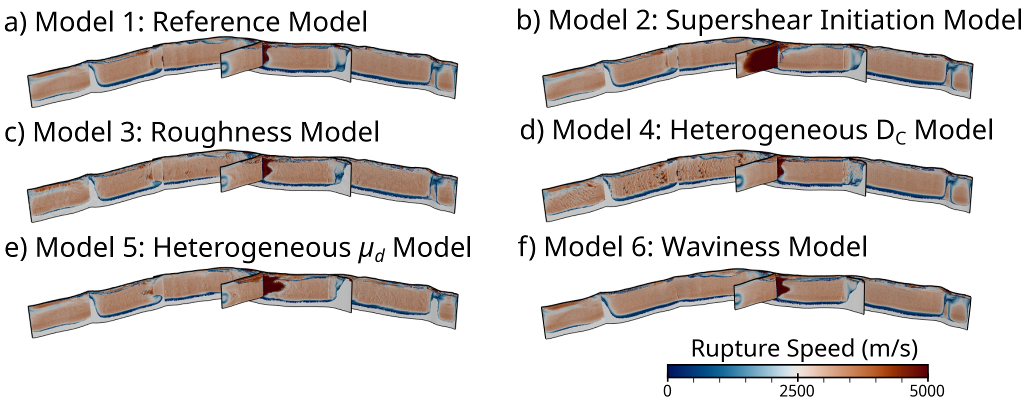

Figure 7: The rupture speed along the fault for the six models explored, where the dark red areas highlight supershear rupture speed.

shear rupture speed is observed in the reference model (Figure 7a and Movie S2a), which is resembled in the supershear initiation model (Figure 7b and Movie S2b) except along the NPF. Perturbations in rupture speed due to geometry and friction heterogeneities are observed in the roughness and μ_d models (Models 3 and 5), where there are local episodic changes in rupture speed across the entire fault system. Similar perturbations that generate episodic supershear rupture speeds are observed in the western segment of the EAF for the D_c model, while the eastern segment exhibits a smoother distribution of subshear rupture speed, similar to that in the reference model. Lastly, the waviness model shows constant rupture speed similar to that in the reference model, with some minimal variations due to how the different segments are triggered, particularly to the west of the NPF-EAF junction.

From Figure 6, we can also observe a correlation between PSR and rupture speed (e.g., Rice et al., 2005; Gabriel et al., 2013). Although the relation viewed here is unclear, the impacted PSR in Model 4 appears on the particular fault segments where transient supershear rupture speeds are observed. This implies that the presence of local transient supershear rupture speeds impacts PSR. We see this in Figure 6a.iv and b.iii in the areas of the previously mentioned rupture speed perturbations along the EAF for the D_c model, oriented at a strike of $\sim 26\ ^\circ$ and $\sim 80\ ^\circ$.

4.2 Long-Period Velocity Pulse Analysis

The pulse analysis described in Section 2.1 is used to investigate the low-frequency regime of all six dynamic rupture models. Figure 8 illustrates the extracted long-period velocity pulses at all near-fault stations. Because each model generates seismograms that differ from the reference model, the number of stations classified as pulse-bearing varies. Supplementary Figure S2 shows the comparison of pulse maps from the Jia et al. (2023) model and the reference model.

Pulse amplitude variability is reproduced consistently across all models. All models generally classify less stations as pulse-like compared to the data (Figure 1a). The reference scenario captures the broad pulse amplitude variability observed in the data, and the additional rupture complexities preserve this behaviour. Differences in the classification of pulse-like stations arise only at a small number of stations, such as the inclusion of the southern station 3123 in the waviness model and the exclusion of station 3131 in the roughness model. The amplitude distributions shown in Figure 9a fall within 50–300 cm/s and follow a spatial trend similar to the Engineering Strong Motion (ESM,

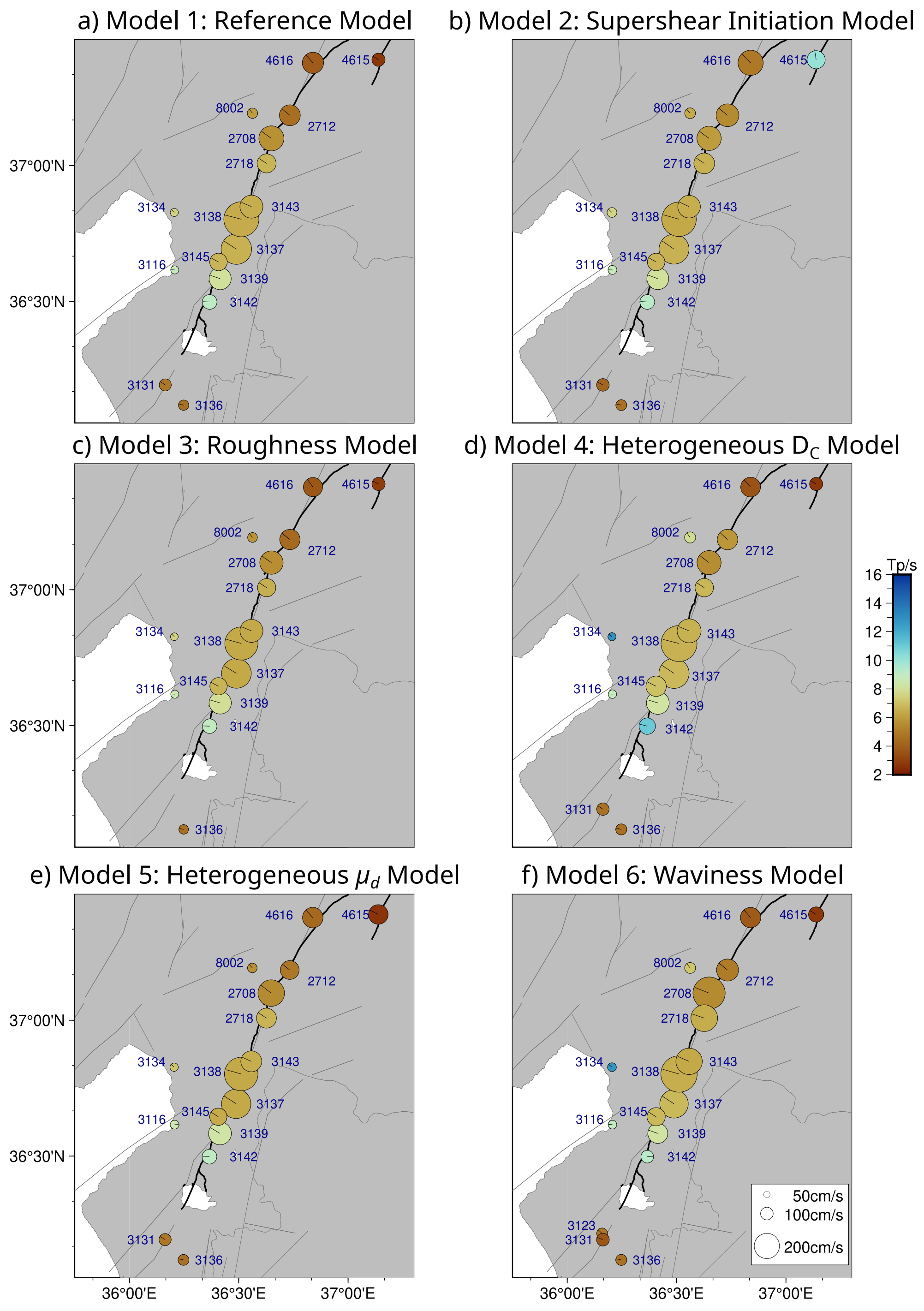

Figure 8: Maps showing velocity pulse properties extracted at various stations for each model. As in Figure 1b, the circle size corresponds to the pulse amplitude, the colour corresponds to the pulse period (T_p), and the lines within the circles represent the pulse orientation. For each model explored, the seismograms at each station differ from those in the reference model, leading to model-dependent variations in the classification of velocity pulses. As a result, each model has a different total number of stations that are classified as containing velocity pulses.

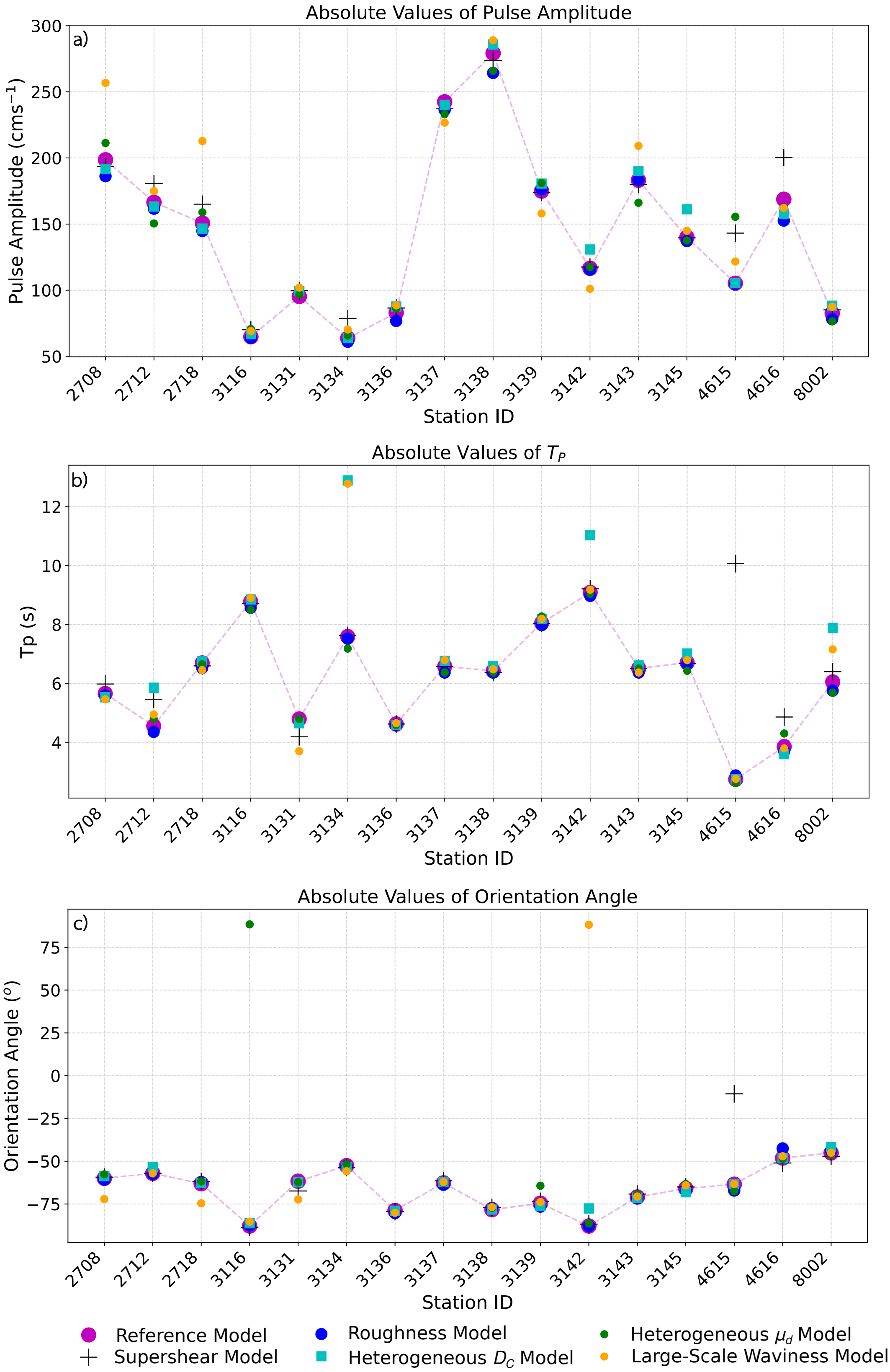

Figure 9: A comparison of a) pulse amplitude, b) pulse period (T_p), and c) pulse orientation for all six models. The pink dotted line represents the reference model variability trend to emphasise differences in models with added variability.

Luzi et al. (2020)) dataset (Figure S5a), with the large-scale waviness model generating the largest divergences from the reference pattern.

Pulse durations, T_p, show modest sensitivity to the added heterogeneities. The reference model produces T_p values between roughly 2-9 s. Supershear initiation, heterogeneous D_c and large-scale waviness broaden this range to approximately 2–13s (Figure 9b). The D_c model leads to the strongest deviations in pulse duration, consistent with its locally episodic supershear behaviour identified in the rupture-speed (Figure 7). These changes remain small compared to the variability inferred from observations.

Pulse orientation remains largely unaffected by the imposed dynamic rupture complexities. Most stations preserve fault normal orientations, as in the reference model. Only three stations (4615 in Model 2, 3116 in Model 5 and 3142 in Model 6) show orientation changes (Figure 9c). The supershear initiation model modifies both T_p and pulse orientation at station 4615, which rotates toward a more fault-parallel orientation and lengthens in period. Two additional changes of pulse orientation involve 180$\circ$ flips at station 3116 and station 3142 in the heterogeneous μ_d and waviness models, respectively. Aside from these isolated examples, the modelled pulse orientation variability is minimal in all models, in contrast to the broader range observed in observational data (Figure S5, M.-H. Yen et al. (2025)).

Overall, our analysis shows that all dynamic rupture models capture pulse amplitude variability well but generate limited variability in pulse periods and orientations. Supershear rupture and large-scale geometric perturbations exert the strongest influence, although their effects remain localised. The systematic lack of orientation variability suggests that additional physical processes, such as off-fault fracturing or path-dependent modifications, may be required to explain the patterns observed in the recordings.

4.3 Higher-Frequency Analysis

We apply spectral analysis to the synthetic seismograms at all stations for each of the six dynamic rupture models. For each three-component velocity time series, we compute Fourier amplitude spectra and compare the spectral shapes and levels across models and stations (Figure S6). In the near-fault high-resolution region, the simulations numerically resolve frequencies slightly above 2 Hz, whereas in the coarser parts of the mesh, the reliable frequency range extends to about 1.5 Hz.

Inspection of the spectra over the total frequency band shows that all models produce similar spectral shapes at both near- (Figure S6c) and far-fault stations (Figure S6d), with comparable low-frequency plateaus and a similar decay at higher frequencies. Small differences in spectral amplitudes occur from station to station but are not systematic between models. Focusing on the near-fault stations and restricting the analysis to 0–1 Hz (Figure S6a,b), the spectra of the six scenarios nearly overlap at most sites, with only modest deviations that are comparable to the spread between components or neighbouring stations. Within this band, the heterogeneous models therefore do not exhibit a clear, model-dependent shift in spectral level or corner frequency relative to the reference case.

This analysis contrasts with the imprint of supershear rupture, roughness, and heterogeneous friction on rupture speed, peak slip rate and rupture dynamics (Figures 4, 7 and 6). This may suggest that the main impact of these complexities would be expressed at frequencies approaching or exceeding the upper limit of our resolved range, (e.g., B. Wu et al., 2025). The small-scale features we introduced in the roughness, D_c, and μ_d models following (e.g., Shi & Day, 2013; Graves & Pitarka, 2016; Taufiqurrahman et al., 2022), do not translate into robust differences in spectral amplitudes below about 1 Hz. Additional variability in higher-frequency ground motions is likely to occur at frequencies beyond those analysed here and would require finer spatial resolution and more detailed attenuation structure to be reliably quantified.

5 Discussion

5.1 Validation of Modelled Long-Period Near-Fault Pulse Characteristics

As detailed in Section 4.2, all heterogeneous dynamic rupture models reproduce the same variability in modelled pulse amplitudes that is produced by the reference model. They follow the same fluctuation patterns, which in turn, on comparing to observed data (Figure S5), align quite well with the variability patterns observed in nature. It is the reference model that appears to perform the most similar to the observed data, whilst the added complexities often cause a deviation from the more optimal variability produced by the reference model. However, all six models appear to overestimate the amplitude values compared to those observed.

On comparing the T_p variability between the models and the observed data, we see that the synthetics produce values between 3 s and 9 s, whereas the observational data show values ranging between 3 s and 15 s, with a very different variability pattern. Although it is understood that the pulse period range is driven by the magnitude of the earthquake (Fayjaloun et al., 2017), other factors are also important, such as the impacts of site effects (Rodriguez-Marek & Bray, 2006).

Figure S5c shows the lack of pulse orientation variability produced by the models compared to what is seen in the observational data, similar to what was observed in M.-H. Yen et al. (2025) using the dynamic rupture model by (Jia et al., 2023). This lack of variability suggests that the heterogeneities studied might, in general, not be the major factors involved in generating the pulse orientation. However, a local impact of supershear rupture speeds on pulse properties is seen at station 4615 for the supershear initiation model. Supershear ruptures have been speculated to be responsible for the generation of near-fault pulse-like motion, as such rupture speeds reshape the S-wave radiation pattern. When rupture speed exceeds the S-wave speed of the host rock, shear dislocation on the fault releases some strain energy as shear Mach wave fronts (Dunham & Bhat, 2008). This may cause most of the near-field seismic energy to arrive in one pulse of motion, expected at the S-wave arrival time (Somerville et al., 1997; Ertruncay & Costa, 2024).

In our results, supershear rupture speed locally impacts the generation of pulse-like motion, resulting in a more variable pulse in both period and orientation in this region of the fault. On comparing the variations in pulse amplitude and orientation with the observed data in Figure S5, we can see that the values for station 4615 for the supershear initiation model are closer to those observed. All other models differ from the observed pulse amplitude at this station by ~ 50 cm/s, while Model 2 only differs by ~ 10 cm/s. Similarly, for the pulse orientation, all other models differ by $\sim 50°$, while Model 2 is closer in orientation, differing by $\sim 10°$. This could support the hypothesis of the likelihood of supershear initiation and propagation along the nucleating NPF (e.g., Abdelmeguid et al., 2023; Delouis et al., 2024; Ren et al., 2024; Rosakis et al., 2025).

On further investigating the impact of the D_c heterogeneities, we can rule out that the cause of the effects on the pulse properties is due to a changing fracture energy via the changes in D_c. If this were the cause, it would imply that similar results should be obtained from the heterogeneous μ_d model, which only affected the pulse orientation at one station. The impact of D_c heterogeneities is most likely linked to the locally episodic supershear rupture along the south-western segment of the EAF (Figure 7). Such supershear bursts are not observed in any of the other models and are most likely responsible for the T_p and amplitude variability generated in Model 4.

As the large-scale waviness model has been designed to introduce a physical on-fault heterogeneity that is comparable to the target long-period characteristics of the pulses, it was expected to influence pulse behaviour. The extent of this model's impact on the pulse period and orientation implies that the waviness wavelengths we use are too large for this target. In the top view of the fault for this model in Figure 2f, the effects of the waviness are minimally observed on a small portion of the south-western end of the EAF. Although the model's influence on the pulse properties could correlate with areas of pronounced waviness on the fault, there is not enough evidence for such a definitive interpretation. This could be further explored through applying waviness wavelengths between 10 - 40 km.

Although the influence of heterogeneities, such as fault roughness and heterogeneous μ_d, on long-period velocity pulses has not been extensively explored, the limited impact observed here is not unexpected. We include these features primarily for their known effects on rupture dynamics and frequency radiation, rather than for an anticipated influence on long-period pulse characteristics (Withers, Olsen, Day, & Shi, 2019; Harris et al., 2018). However, within the resolved frequency range of up to ~ 1 Hz, no individual model exhibits distinctly higher spectral amplitudes, with the overall frequency content remaining broadly similar across models. This is somewhat unexpected, given the established role of fault roughness and heterogeneous μ_d, and reflects limitations imposed by numerical resolution or the specific parameterisation adopted here. Despite this, Models 3 and 5 exhibiting a reduced moment rate release (Figure 4) and lower seismic moment (Table 2) suggests that there is additional resistance to rupture propagation and that more energy is therefore required to overcome these heterogeneities. This can be interpreted as an expression of roughness drag acting on the fault (Fang & Dunham, 2013). Therefore, although such heterogeneities do not strongly control long-period pulse characteristics in the present simulations, they nonetheless exert a measurable influence on rupture propagation. Furthermore, fault roughness has been seen to distort the radiation pattern, due to stress concentrations that create local barriers to rupture propagation, which in turn lower rupture directivity and decrease ground-motion variability (Vyas et al., 2024).

5.2 Off-Fault Fracture Networks

To explore the possibilities of off-fault implications to the variability generated in the pulses, we ran the pulse analysis on the outputs from a suite of simulations with off-fault fracture networks published in Gabriel et al. (2024), which have a similar setup to those analysed in (Palgunadi et al., 2024, 2025). Geological faults evolve into complex systems characterised by multiscale features, including volumetric fracture networks and complex damage zones (e.g., W. L. Power & Tullis, 1991; Ben-Zion & Sammis, 2003; Bhat et al., 2007; Candela et al., 2010; Faulkner et al., 2010; Mitchell & Faulkner, 2009; Savage & Brodsky, 2011; Griffith et al., 2012; Ostermeijer et al., 2022). Off-fault distributed damage and localised fractures affect on-fault rupture dynamics, as well as seismic radiation (Madariaga, 1977; D. Andrews, 2005; Okubo et al., 2019; Gabriel et al., 2021; Zhao et al., 2024; B. Wu et al., 2025). Gabriel et al. (2024) use a suite of 3D dynamic rupture models on an 8 km east-west vertical strike-slip fault, buried at a depth of 1 km, with more than 700 multiscale off-fault fractures within a fault damage zone, embedded in an elastic half-space. These fractures are divided into two families oriented at an average strike of 25 ° and -65 °, and an average dip of 90 ° with a standard deviation of $\pm 10°$. They are elliptical disks, with the majority connected to at least one fracture. The models use a linear scaling relationship between fracture energy (D_c) and fault/fracture size, derived from physics-based corrections for seismologically observed fracture energy to estimate the total earthquake fracture energy across a range of rupture sizes.

Cases 3 and 4 use the main-fault fracture network dynamic rupture modelling setup as seen in Figure 10a. Case 3 involves a heterogeneous setup of fault size-dependent fracture energy, whereas case 4 assumes a uniformly large fracture energy for the main fault and all fractures. Therefore, case 4 results in slip on the main fault but not on the fracture network, producing a M_w 5.94 seismic event. Case 3 involves closer-to-critical pre-

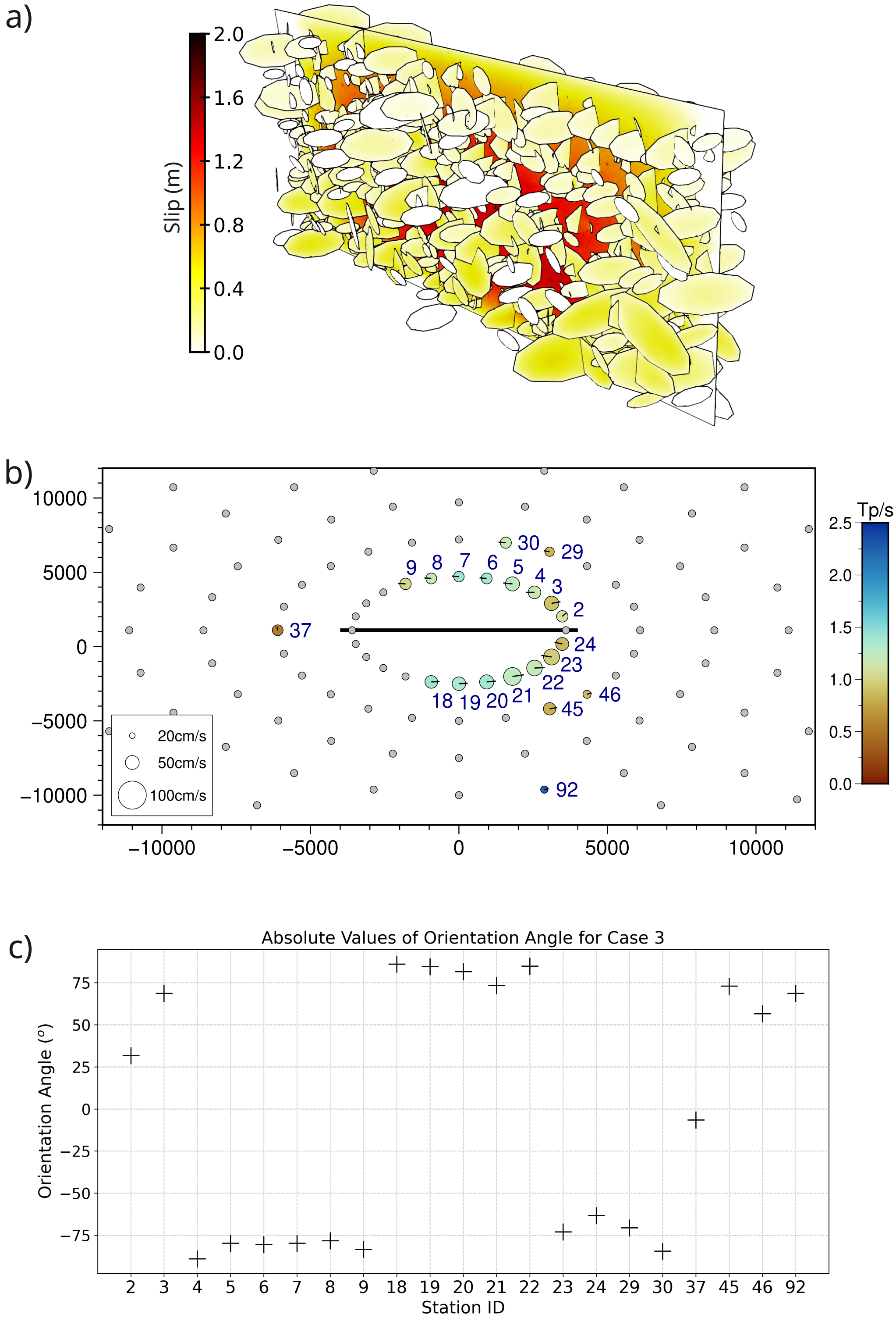

Figure 10: Pulse analysis results from the case 3 fracture network setup of Gabriel et al. (2024). a) The case 3 fracture network setup. b) Pulse map, similar to Figure 1b, highlighting the extracted pulse properties for case 3. The map focuses on the stations classified as pulse-like. Hence, the grey circles represent the stations that have not been classified as containing a pulse. c) Plot showing the variability in pulse orientation.

stress conditions, resulting in an earthquake cascade along the fracture network that dynamically triggers the main fault to re-rupture after 2.1 s, generating a M_w 6 seismic event.

Our new analysis here shows that the inclusion of a fracture network adds variability to the generated pulses, particularly to the pulse orientation. As depicted in Figure 10b and c, for a fault oriented W-E, the pulse orientations vary from the fault-normal orientations (0° and 180°), averaging around 75^0 and -75^0. Slip occurring on both the fracture network and the main fault in case 3 is responsible for the slightly larger earthquake. This produces more pulse-like motion than in case 4 (Figure S7), which only has 3 pulse-like stations. The presence of an activated fracture network in case 3 generates variability in the pulse orientations compared to what is seen in the six models explored in this study. From observing mostly fault normal pulse orientations in all our models of the Kahramanmaraş earthquake (Figure 8), we now observe predominantly fault parallel orientations that flip polarity as the station locations move from north of the fault to south of the fault. These orientations appear to follow the left-lateral strike-slip motion of the main fault rupture. We also see increased variability in the pulse amplitudes, ranging from around 25 - 65 cm/s (Figure S8a), and some variability in T_p, ranging from 0.5 - 2.25 s (Figure S8b). Since the period is mainly driven by the magnitude of the earthquake (Shahi & Baker, 2011; Fayjaloun et al., 2017), we expect a lower range of T_p variation for a M_w 6 seismic event (Shahi & Baker, 2014). However, these values are at the lower end of typical ranges of periods observed for such magnitudes, even though this is highly variable (M. Yen et al., 2021; Türker et al., 2023).

Compared with Figures S7 and S8 for case 4, the impact of a fracture network can be clearly seen. Case 4 involved only the rupturing of the main fault and only generated 3 stations as pulse-like. These 3 stations have lower amplitudes and amplitude variability (~ 43 and ~ 50 cm/s), very short periods (0.25 - 0.6 s) and only fault normal pulse orientations at the ends of the fault where the directivity effects are strongest (Spudich & Chiou, 2008; Somerville et al., 1997). We see similar behaviour at station 37 between the two cases. The pulse extracted at this station has a similar amplitude, period and orientation in both cases. These results highlight the impact of off-fault fracture network rupture, primarily generating variability in the pulse orientations.

5.3 Limitations and Future Work

The limited impact on pulse period from our heterogeneous dynamic rupture models could be related to a few additional aspects not discusses above. The first potential problem could be omitting site effects, even though the earthquake is located in a basin area. There have been a number of studies on the site effects due to the basin sediment in the area that show that these can have an amplification effect on the amplitudes and periods of such long-period pulses (e.g., Rodriguez-Marek & Bray, 2006; Koketsu et al., 2016; M. Yen et al., 2021; Ertruncay & Costa, 2024). M.-H. Yen et al. (2025) showed that site effects can interact with near-field directivity effects when the pulse period is close to the site's dominant frequency. These effects may interact mutually or solely affect pulse generation (Cork et al., 2016; Kaneko & Goto, 2022; Cao et al., 2025), potentially leading to significant variability in pulse properties. The basin sediments have not been taken into consideration in this study due to the limited availability of 3D velocity models. In future work, this could be improved through the use of a more detailed 3D velocity model (Li et al., 2025) or through a correction for site effects on the synthetic signals as an extension of the concepts in Rodgers et al. (2020).

Another difficulty is properly representing the fault system geometry. It is very challenging to know the precise fault geometry beyond what is obtainable through geodetic and aftershock data, specifically at depth. Since this was not explored in this study, using an even more detailed, complex fault geometry, for example, one that includes more step-overs or larger variations in fault dip, would be interesting (Shahi & Baker, 2011;

Lozos et al., 2025). Furthermore, it is possible that some of the observed pulse orientation variability is due to the potential misalignment of stations and the overturning of instruments during the strong shaking, such as station 3138 (Ertruncay & Costa, 2024; M.-H. Yen et al., 2025).

6 Conclusions

We investigate whether different forms of on-fault complexity in 3D dynamic rupture simulations can reproduce the observed variability of long-period near-fault velocity pulses during the 2023 M_w 7.8 Kahramanmaraş earthquake. To this end, we design a suite of rupture scenarios in which we vary fault roughness, large-scale waviness, heterogeneous fracture energy, and supershear versus subshear initiation, while maintaining comparable seismic moment rate release and moment magnitude, and reasonable fit to observed near-fault long-period velocity pulse amplitude variability. Across the tested on-fault heterogeneities, we mostly do not observe a systematic increase in variability in modelled long-period velocity pulse orientations. In distinctions, local supershear rupture speeds, when present near a station, affect pulse orientation and period, and may be a primary driver of the commonly observed long-period pulse variability. Overall, the modelled pulses remain predominantly fault-normal in most of our scenarios, implying that the orientation variability seen in observations may not be reproduced by on-fault heterogeneity alone. A comparison with generic dynamic rupture models that include an off-fault fracture-network points to off-fault processes as an efficient pathway to increasing variability in pulse orientation (and, secondarily, amplitude). This is consistent with earlier work showing that damage-zone structure and distributed inelastic deformation can reshape near-fault radiation patterns beyond what is captured by modelling the main fault rupture dynamics only, with important implications for physics-based, non-ergodic ground motion models accounting for near-fault long-period velocity pulses.

Open Research Section

The dynamic rupture simulations were performed using SeisSol (`www.seissol.org`), an open-source software freely available to download from `https://github.com/SeisSol/SeisSol/`. We use SeisSol, commit 01ae1b1. All data required to reproduce the dynamic rupture scenarios (i.e. computational mesh and SeisSol input files) can be downloaded from the Zenodo repository (Preca Trapani et al., 2025). Instructions for downloading, installing, and running the code are available in the SeisSol documentation at `https://seissol.readthedocs.io/`. Downloading and compiling instructions are at `https://seissol.readthedocs.io/en/latest/build-seissol.html`. Instructions for setting up and running simulations are at `https://seissol.readthedocs.io/en/latest/configuration.html`. Quickstart containerized installations and introductory materials are provided in the Docker container and Jupyter notebooks at `https://github.com/SeisSol/Training`. Example problems and model configuration files are provided at `https://github.com/SeisSol/Examples`, many of which reproduce the SCEC 3D Dynamic Rupture benchmark problems described at `https://strike.scec.org/cvws/benchmark_descriptions.html`. The pulse analysis code can be downloaded from `https://github.com/shocky0424/PulseClassification`. Strong ground motion data were downloaded from the ESM Database `https://esm-db.eu/#/home`. The nucleation location was taken from the Disaster and Emergency Management Authority (AFAD) database of Türkiye `https://deprem.afad.gov.tr/event-detail/408326`. Maps were generated using Generic Mapping Tools v.6.5.0 (Wessel et al., 2019).

Conflict of Interest

The authors declare no conflicts of interest relative to this study.

Acknowledgments

We are thankful to Thomas Ulrich for his help in troubleshooting the SeisSol models, as well as Oona Scotti and Sebastien Hok for valuable discussions. This work received funding from the European Union's Horizon 2020 research and innovation programme under the Marie-Sklodowska-Curie grant agreement No. 101072699 - TREAD-ITN (https://tread-horizon.eu/), Horizon Europe (Geo-INQUIRE, grant no. 101058518, DT-Geo, grant no. 101058129, and ChEESE-2P, 101093038), NSF (grants no. EAR-2143413, EAR-2121568, OAC-2139536, OAC-2311208, RISE-2531036), and NASA (grant no. 80NSSC20K0495). B. W. acknowledges additional support from the IGPP Green's Foundation. The authors acknowledge the Gauss Centre for Supercomputing e.V. for providing computing time on the supercomputer SuperMUC-NG at the Leibniz Supercomputing Centre (www.lrz.de) in project pn49ha. Additional computing resources were provided by the Institute of Geophysics of LMU Munich (Oeser et al., 2006).

References

Abdelmeguid, M., Zhao, C., Yalcinkaya, E., Gazetas, G., Elbanna, A., & Rosakis, A. (2023). Dynamics of episodic supershear in the 2023 m7.8 kahramanmaraş/pazarcik earthquake, revealed by near-field records and computational modeling. *Communications Earth and Environment*, *4*(456). doi: https://doi.org/10.1038/s43247-023-01131-7

Akinci, A., Dindar, A. A., Bal, I. E., Ertuncay, D., Smyrou, E., & Cheloni, D. (2025). Characteristics of strong ground motions and structural damage patterns from the february 6th, 2023 kahramanmaraş earthquakes, türkiye. *Natural Hazards*, *121*, 1209–1239. Retrieved from `https://doi.org/10.1007/s11069-024-06856-y` doi: 10.1007/s11069-024-06856-y

Anderson, E. M. (1905). The dynamics of faulting. *Transactions of the Edinburgh Geological Society*, *8*(3), 387–402.

Anderson, E. M. (1951). *The dynamics of faulting and dyke formation with applications to britain* (2nd ed.). Edinburgh: Oliver and Boyd.

Andrews, D. (2005). Rupture dynamics with energy loss outside the slip zone. *Journal of Geophysical Research: Solid Earth*, *110*(B1). doi: 10.1029/2004JB003191

Andrews, D. J. (1976). Rupture propagation with finite stress in antiplane strain. *Journal of Geophysical Research*, *81*(32), 3575-3582. doi: 10.1029/JB081i032p05679

Aochi, H., & Madariaga, R. (2003). The 1999 izmit, turkey, earthquake: Nonplanar fault structure, dynamic rupture process, and strong ground motion. *Bulletin of the Seismological Society of America*, *93*(3), 1249–1266.

Baker, J. W. (2007, October). Quantitative classification of near-fault ground motions using wavelet analysis. *Bulletin of the Seismological Society of America*, *97*(5), 1486–1501. Retrieved from `https://doi.org/10.1785/0120060255` doi: 10.1785/0120060255

Baltzopoulos, G., Baraschino, R., Chioccarelli, E., Cito, P., Vitale, A., & Iervolino, I. (2023). Near-source ground motion in the m7. 8 gaziantep (turkey) earthquake. *Earthquake Engineering & Structural Dynamics*, *52*(12), 3903–3912. Retrieved from `https://doi.org/10.1002/eqe.3939` doi: 10.1002/eqe.3939

Barbot, S., Luo, H., Wang, T., Hamiel, Y., Piatibratova, O., Javed, M. T., … Gurbuz, G. (2023). Slip distribution of the february 6, 2023 mw 7.8 and mw 7.6, kahramanmaraş, turkey earthquake sequence in the east anatolian fault zone. *Seismica*, *2*(3), 1–15. Retrieved from `https://doi.org/10.26443/seismica.v2i3.502` doi: 10.26443/seismica.v2i3.502

Ben-Zion, Y., & Sammis, C. G. (2003). Characterization of fault zones. *Pure Appl. Geophys.*, *160*, 677–715.

Bhat, H. S., Olives, M., Dmowska, R., & Rice, J. R. (2007). Role of fault branches in earthquake rupture dynamics. *J. Geophys. Res. Solid Earth*, *112*(B11), B11309–B11325.

Bizzarri, A. (2010, 05). How to promote earthquake ruptures: Different nucleation strategies in a dynamic model with slip-weakening friction. *Bulletin of The Seismological Society of America - BULL SEISMOL SOC AMER*, *100*. doi: 10.1785/0120090179

Bizzarri, A., & Spudich, P. (2008). Effects of supershear rupture speed on the high-frequency content of s waves investigated using spontaneous dynamic rupture models and isochrone theory. *Journal of Geophysical Research: Solid Earth*, *113*(B5). doi: 10.1029/2007JB005146

Bommer, J. J., Abrahamson, N. A., Strasser, F. O., Pecker, A., Bard, P.-Y., et al. (2004). The challenge of defining upper bounds on earthquake ground motions. *Seismological Research Letters*, *75*(1), 82–95. doi: 10.1785/gssrl.75.1.82

Bray, J. D., & Rodriguez-Marek, A. (2004). Characterization of forward-directivity ground motions in the near-fault region. *Soil Dynamics and Earthquake Engineering*, *24*(11), 815–828. doi: 10.1016/j.soildyn.2004.05.001

Breuer, A., Heinecke, A., Rettenberger, S., Bader, M., Gabriel, A.-A., & Pelties, C. (2014). Sustained petascale performance of seismic simulations with seissol on supermuc. In *Proceedings of the international supercomputing conference* (pp. 1–18). Cham: Springer International Publishing. doi: 10.1007/978-3-319-07518-1_1

Candela, T., Renard, F., Bouchon, M., Brouste, A., Marsan, D., Schmittbuhl, J., & Voisin, C. (2009). Characterization of fault roughness at various scales: Implications of three-dimensional high resolution topography measurements. In *Mechanics, structure and evolution of fault zones* (pp. 1817–1851). Springer. doi: 10.1007/s00024-009-0521-2

Candela, T., Renard, F., Bouchon, M., Brouste, A., Marsan, D., Schmittbuhl, J., & Voisin, C. (2010). Characterization of fault roughness at various scales: Implications of three-dimensional high resolution topography measurements. *Pure Appl. Geophys.*, *166*, 1817–1851.

Candela, T., Renard, F., Klinger, Y., Mair, K., Schmittbuhl, J., & Brodsky, E. E. (2012). Roughness of fault surfaces over nine decades of length scales. *Journal of Geophysical Research: Solid Earth*, *117*(B8). doi: 10.1029/2011JB009041

Cao, Z., Wei, J., Sun, Z., & Song, W. (2025). Spatial characteristic analysis of near-fault velocity pulses based on simulation of earthquake ground motion fields. *Buildings*, *15*(8), 1363. doi: https://doi.org/10.3390/buildings15081363

Chang, Z., Wu, H., Li, W., Yan, Z., Peng, L., & Zhu, G. (2025). Analysis of near-fault ground motions in the february 2023 kahramanmaraş, türkiye, earthquake sequence. *Bulletin of Earthquake Engineering*, *23*, 1349–1369. Retrieved from `https://doi.org/10.1007/s10518-025-02101-4` doi: 10.1007/s10518-025-02101-4

Chioccarelli, E., & Iervolino, I. (2010). Near-source seismic demand and pulse-like records: A discussion for l'aquila earthquake. *Earthquake Engineering & Structural Dynamics*, *39*(9), 1039–1062. doi: https://doi.org/10.1002/eqe.987

Cork, T. G., Kim, J. H., Mavroeidis, G. P., Kim, J. K., Halldorsson, B., & Papageorgiou, A. S. (2016). Effects of tectonic regime and soil conditions on the pulse period of near-fault ground motions. *Soil Dynamics and Earthquake Engineering*, *80*, 102–118. doi: https://doi.org/10.1016/j.soildyn.2015.09.011

Das, S., & Aki, K. (1977, 09). A numerical study of two-dimensional spontaneous rupture propagation. *Geophysical Journal International*, *50*(3), 643-668. Retrieved from `https://doi.org/10.1111/j.1365-246X.1977.tb01339.x` doi: 10.1111/j.1365-246X.1977.tb01339.x

Daubechies, I. (1993). Orthonormal bases of compactly supported wavelets ii. variations on a theme. *SIAM journal on mathematical analysis*, *24*(2), 499–519.

Day, S. M. (1982, December). Three-dimensional simulation of spontaneous rupture:

The effect of nonuniform prestress. *Bulletin of the Seismological Society of America*, *72*(6A), 1881–1902. Retrieved 2024-02-07, from https://doi.org/10.1785/BSSA07206A1881 doi: 10.1785/BSSA07206A1881

Delouis, B., van den Ende, M., & Ampuero, J.-P. (2024). Kinematic rupture model of the february 6th 2023 mw7.8 turkey earthquake from a large set of near-source strong motion records combined with gnss offsets reveals intermittent supershear rupture. *Bulletin of the Seismological Society of America*, *114*(2), 726–741. Retrieved from https://doi.org/10.1785/0120230077 doi: 10.1785/0120230077

Dumbser, M., & Käser, M. (2006). An arbitrary high-order discontinuous galerkin method for elastic waves on unstructured meshes — ii. the three-dimensional isotropic case. *Geophysical Journal International*, *167*(1), 319–336. doi: 10.1111/j.1365-246X.2006.03120.x

Dunham, E. M., Belanger, D., Cong, L., & Kozdon, J. E. (2011). Earthquake ruptures with strongly rate-weakening friction and off-fault plasticity, part 2: Nonplanar faults. *Bulletin of the Seismological Society of America*, *101*(5), 2308–2322. doi: 10.1785/0120100076

Dunham, E. M., & Bhat, H. S. (2008). Attenuation of radiated ground motion and stresses from three-dimensional supershear ruptures. *Journal of Geophysical Research: Solid Earth*, *113*(B8). doi: https://doi.org/10.1029/2007JB005182

Ertruncay, D., & Costa, G. (2024). Analysis of impulsive ground motions from february 2023 kahramanmaraş earthquake sequence. *Bulletin of Earthquake Engineering*, *23*, 965–999. doi: https://doi.org/10.1007/s10518-024-01897-x

Fang, Z., & Dunham, E. M. (2013). Additional shear resistance from fault roughness and stress levels on geometrically complex faults. *Journal of Geophysical Research: Solid Earth*, *118*(7), 3642–3654. doi: 10.1002/jgrb.50262

Farr, T. G., Rosen, P. A., Caro, E., Crippen, R., Duren, R., Hensley, S., ... Alsdorf, D. (2007). The shuttle radar topography mission. *Reviews of Geophysics*, *45*(2). doi: https://doi.org/10.1029/2005RG000183

Faulkner, D., Jackson, C., Lunn, R., Schlische, R., Shipton, Z., Wibberley, C., & Withjack, M. (2010). A review of recent developments concerning the structure, mechanics and fluid flow properties of fault zones. *J. Struct. Geol.*, *32*(11), 1557–1575. doi: 10.1016/j.jsg.2010.06.009

Fayjaloun, R., Causse, M., Voisin, C., Cornou, C., & Cotton, F. (2017). Spatial variability of the directivity pulse periods observed during an earthquake. *Bulletin of the Seismological Society of America*, *107*(1), 308–318. doi: 10.1785/0120160199

Gabriel, A.-A., Ampuero, J.-P., Dalguer, L., & Mai, P. M. (2013). Source properties of dynamic rupture pulses with off-fault plasticity. *Journal of Geophysical Research: Solid Earth*, *118*(8), 4117–4126. doi: 10.1002/jgrb.50213

Gabriel, A.-A., Ampuero, J.-P., Dalguer, L. A., & Mai, P. M. (2012). The transition of dynamic rupture styles in elastic media under velocity-weakening friction. *Journal of Geophysical Research: Solid Earth*, *117*(B9). Retrieved from https://agupubs.onlinelibrary.wiley.com/doi/abs/10.1029/2012JB009468 doi: https://doi.org/10.1029/2012JB009468

Gabriel, A.-A., Garagash, D. I., Palgunadi, K. H., & Mai, P. M. (2024). Fault size–dependent fracture energy explains multiscale seismicity and cascading earthquakes. *Science*, *385*(6707), eadj9587. doi: 10.1126/science.adj9587

Gabriel, A.-A., Kurapati, V., Niu, Z., Schliwa, N., Schneller, D., Ulrich, T., ... Bader, M. (2025, June). *Seissol.* Zenodo. Retrieved from https://doi.org/10.5281/zenodo.15685917 doi: 10.5281/zenodo.15685917

Gabriel, A.-A., Li, D., Chiocchetti, S., Tavelli, M., Peshkov, I., Romenski, E., & Dumbser, M. (2021). A unified first-order hyperbolic model for nonlinear dynamic rupture processes in diffuse fracture zones. *Phil. Trans. R. Soc. A*, *379*(2196), 20200130. doi: 10.1098/rsta.2020.0130

Gabriel, A.-A., Ulrich, T., Marchandon, M., Biemiller, J., & Rekoske, J. (2023, 12). 3d dynamic rupture modeling of the 6 february 2023, kahramanmaraş, turkey mw 7.8 and 7.7 earthquake doublet using early observations. *The Seismic Record*, *3*(4), 342-356.
Galis, M., Pelties, C., Kristek, J., Moczo, P., Ampuero, J.-P., & Mai, P. M. (2015). On the initiation of sustained slip-weakening ruptures by localized stresses. *Geophysical Journal International*, *200*(2), 890–909. doi: 0.1093/gji/ggu436
Gallovič, F., & Ľ. Valentová. (2023). Broadband strong ground motion modeling using planar dynamic rupture with fractal parameters. *Journal of Geophysical Research: Solid Earth.* (First published: 16 May 2023) doi: 10.1029/2023JB026506
Galvez, P., Ampuero, J.-P., Dalguer, L. A., Somala, S. N., & Nissen-Meyer, T. (2014). Dynamic earthquake rupture modelled with an unstructured 3-d spectral element method applied to the 2011 m 9 tohoku earthquake. *Geophysical Journal International*, *198*(2), 1222–1240. doi: 10.1093/gji/ggu203
Graves, R., & Pitarka, A. (2016). Kinematic ground-motion simulations on rough faults including effects of 3d stochastic velocity perturbations. *Bulletin of the Seismological Society of America*, *106*(5), 2136–2153. Retrieved from `https://doi.org/10.1785/0120160088` doi: 10.1785/0120160088
Griffith, W. A., Mitchell, T. M., Renner, J., & Di Toro, G. (2012). Coseismic damage and softening of fault rocks at seismogenic depths. *Earth Planet. Sci. Lett.*, *353*, 219–230.
Güvercin, S. E., Karabulut, H., Konca, A. O., Doğan, U., & Ergintav, S. (2022). Active seismotectonics of the east anatolian fault. *Geophysical Journal International*, *230*(1), 50–69. doi: https://doi.org/10.1093/gji/ggac045
Harris, R. A., & Abrahamson, N. A. (2014). Strong ground motions generated by earthquakes on creeping faults. *Geophysical Research Letters*, *41*(11), 3774–3780. doi: 10.1002/2014GL060228
Harris, R. A., Barall, M., Aagaard, B., Ma, S., Roten, D., Olsen, K., … others (2018). A suite of exercises for verifying dynamic earthquake rupture codes. *Seismological Research Letters*, *89*. doi: 10.1785/0220170222
Heaton, T. H., Hall, J. F., Wald, D. J., & Halling, M. W. (1995). Response of high-rise and base-isolated buildings to hypothetical mw 7.0 blind thrust earthquake. *Science*, *267*, 206–211. Retrieved from `https://doi.org/10.1126/science.267.5195.206` doi: 10.1126/science.267.5195.206
Heidbach, O., Tingay, M., Barth, A., Reinecker, J., Kurfeß, D., & Müller, B. (2010). Global crustal stress pattern based on the world stress map database release 2008. *Tectonophysics*, *482*(1-4), 3–15. doi: 10.1016/j.tecto.2009.07.023
Heinecke, A., Breuer, A., Rettenberger, S., Bader, M., Gabriel, A.-A., Pelties, C., … Dubey, P. (2014, Nov.). Petascale high order dynamic rupture earthquake simulations on heterogeneous supercomputers. In *Sc '14: Proceedings of the international conference for high performance computing, networking, storage and analysis.* doi: 10.1109/SC.2014.6
Hu, Z., Olsen, K. B., & Day, S. M. (2022). 0–5 Hz deterministic 3-D ground motion simulations for the 2014 La Habra, California, Earthquake. *Geophysical Journal International*, *230*, 2162–2182. (Advance Access publication 2022 May 10) doi: 10.1093/gji/ggac174
Ida, Y. (1972). Cohesive force across the tip of longitudinal-shear crack and griffth's specific surface energy. *Journal of Geophysical Research*, *77*(20), 3796-3805. doi: 10.1029/jb077i020p03796
Ide, S., & Aochi, H. (2005). Earthquakes as multiscale dynamic ruptures with heterogeneous fracture surface energy. *Journal of Geophysical Research: Solid Earth*, *110*(B11). doi: https://doi.org/10.1029/2004JB003591
Jia, Z., Jin, Z., Marchandon, M., Ulrich, T., Gabriel, A.-A., Fan, W., … Fialko, Y. (2023, 08). The complex dynamics of the 2023 kahramanmaraş, turkey, mw

7.8-7.7 earthquake doublet. *Science (New York, N.Y.)*, *381*, eadi0685. doi: https://doi.org/10.1126/science.adi0685

Kaneko, Y., & Goto, H. (2022). The origin of large, long-period near-fault ground velocities during surface-breaking strike-slip earthquakes. *Geophysical Research Letters*, *49*(10). Retrieved from https://agupubs.onlinelibrary.wiley.com/doi/abs/10.1029/2022GL098029 doi: https://doi.org/10.1029/2022GL098029

Koketsu, K., Miyake, H., Guo, Y., Kobayashi, H., Masuda, T., et al. (2016). Widespread ground motion distribution caused by rupture directivity during the 2015 gorkha, nepal earthquake. *Scientific Reports*, *6*, 28536. doi: 10.1038/srep28536

Krenz, L., Uphoff, C., Ulrich, T., Gabriel, A.-A., Abrahams, L. S., Dunham, E. M., & Bader, M. (2021). 3d acoustic-elastic coupling with gravity: The dynamics of the 2018 palu, sulawesi earthquake and tsunami. In *The international conference for high performance computing, networking, storage and analysis.* Association for Computing Machinery. doi: 10.1145/3458817.3476173

Li, B., Palgunadi, K. H., Wu, B., Suhendi, C., Zhou, Y., Ghosh, A., & Mai, P. M. (2025). Rupture dynamics and velocity structure effects on ground motion during the 2023 türkiye earthquake doublet. *Communications Earth & Environment*, *6*(1), 228. doi: 10.1038/s43247-025-02205-4

Li, B., Wu, B., Bao, H., Oglesby, D. D., Ghosh, A., Gabriel, A.-A., … Chu, R. (2022). Rupture heterogeneity and directivity effects in back-projection analysis. *Journal of Geophysical Research: Solid Earth*, *127*(3), e2021JB022663. doi: 0.1029/2021JB022663

Lin, P.-S., Chiou, B., Abrahamson, N., Walling, M., Lee, C.-T., & Cheng, C.-T. (2011). *Repeatable source, site, and path effects on the standard deviation for empirical ground-motion prediction models* (Journal Article No. 101(5)). U.S. Geological Survey. doi: 10.1785/0120090312

Lozos, J., Akçiz, S., & Ladage, H. (2025). Modeling the rupture dynamics of strong ground motion (¿ 1 g) in fault stepovers. *Tectonophysics*, *895*, 230580. Retrieved from https://doi.org/10.1016/j.tecto.2024.230580 doi: 10.1016/j.tecto.2024.230580

Luzi, L., Lanzano, G., Felicetta, C., D'Amico, M. C., Russo, E., Sgobba, S., … 5, O. W. G. (2020). *Engineering strong motion database (esm), version 2.0.* Istituto Nazionale di Geofisica e Vulcanologia (INGV). Retrieved from https://doi.org/10.13127/ESM.2 doi: 10.13127/ESM.2

Madariaga, R. (1977, 12). High-frequency radiation from crack (stress drop) models of earthquake faulting. *Geophysical Journal International*, *51*(3), 625-651. Retrieved from https://doi.org/10.1111/j.1365-246X.1977.tb04211.x doi: 10.1111/j.1365-246X.1977.tb04211.x

Madden, E. H., Ulrich, T., & Gabriel, A.-A. (2022). The state of pore fluid pressure and 3-d megathrust earthquake dynamics. *Journal of Geophysical Research: Solid Earth*, *127*(4). doi: https://doi.org/10.1029/2021JB023382

Mai, P. M., Aspiotis, T., Aquib, T. A., Cano, E. V., Castro-Cruz, D., Espindola-Carmona, A., … others (2023). The destructive earthquake doublet of 6 february 2023 in south-central türkiye and northwestern syria: Initial observations and analyses. *The Seismic Record*, *3*(2), 105–115. Retrieved from https://doi.org/10.1785/0320230007 doi: 10.1785/0320230007

Marchandon, M., Gabriel, A.-A., Chiaraluce, L., Tinti, E., Casarotti, E., & Biemiller, J. (2025). Forecasting 3d rupture dynamics of the alto tiberina low-angle normal fault, italy. *Seismica*, *4*(2). doi: 10.26443/seismica.v4i2.1603

Melgar, D., Taymaz, T., Ganas, A., Crowell, B. W., Öcalan, T., Kahraman, M., … Altuntaş, C. (2023). Sub- and super-shear ruptures during the 2023 mw 7.8 and mw 7.6 earthquake doublet in se türkiye. *Seismica*, *2*(3), 1–10. Retrieved from https://doi.org/10.26443/seismica.v2i3.387 doi:

10.26443/seismica.v2i3.387

Mitchell, T., & Faulkner, D. (2009). The nature and origin of off-fault damage surrounding strike-slip fault zones with a wide range of displacements: A field study from the Atacama fault system, northern Chile. *J. Struct. Geol.*, *31*(8), 802–816. doi: 10.1016/j.jsg.2009.05.002

Okubo, K., Bhat, H. S., Rougier, E., Marty, S., Schubnel, A., Lei, Z., … Klinger, Y. (2019). Dynamics, radiation, and overall energy budget of earthquake rupture with coseismic off-fault damage. *J. Geophys. Res. Solid Earth*, *124*(11), 11771–11801. doi: 10.1029/2019JB017304

Ostermeijer, G. A., Aben, F. M., Mitchell, T. M., Rockwell, T. K., Rempe, M., & Farrington, K. (2022). Evolution of co-seismic off-fault damage towards pulverisation. *Earth and planetary science letters*, *579*, 117353.

Ozkula, G., Dowell, R. K., Baser, T., Lin, J.-L., Numanoglu, O. A., Ilhan, O., … Uludag, T. D. (2023). Field reconnaissance and observations from the february 6, 2023, turkey earthquake sequence. *Natural Hazards*, *119*(1), 663–700. Retrieved from `https://doi.org/10.1007/s11069-023-06143-2` doi: 10.1007/s11069-023-06143-2

Palgunadi, K. H., Gabriel, A.-A., Garagash, D. I., Ulrich, T., & Mai, P. M. (2024). Rupture dynamics of cascading earthquakes in a multiscale fracture network. *Journal of Geophysical Research: Solid Earth*, *129*(3), e2023JB027578. doi: 10.1029/2023JB027578

Palgunadi, K. H., Gabriel, A.-A., Garagash, D. I., Ulrich, T., Schliwa, N., & Mai, P. M. (2025). Ground-motion characteristics of cascading earthquakes in a multiscale fracture network. *Bulletin of the Seismological Society of America*. doi: https://doi.org/10.1785/0120240281

Palmer, A. C., Rice, J. R., & Hill, R. (1973). The growth of slip surfaces in the progressive failure of over-consolidated clay. *Proceedings of the Royal Society of London. A. Mathematical and Physical Sciences*, *332*(1591), 527-548. Retrieved from `https://royalsocietypublishing.org/doi/abs/10.1098/rspa.1973.0040` doi: 10.1098/rspa.1973.0040

Pelties, C., de la Puente, J., Ampuero, J.-P., Brietzke, G. B., & Käser, M. (2012). Three-dimensional dynamic rupture simulation with a high-order discontinuous galerkin method on unstructured tetrahedral meshes. *Journal of Geophysical Research: Solid Earth*, *117*(B2), B02309. doi: 10.1029/2011JB008857

Pelties, C., Gabriel, A.-A., & Ampuero, J.-P. (2014). Verification of an ader-dg method for complex dynamic rupture problems. *Geoscientific Model Development*, *7*(3), 847–866. doi: 10.5194/gmd-7-847-2014

Power, W., Tullis, T., Brown, S., Boitnott, G., & Scholz, C. (1987). Roughness of natural fault surfaces. *Geophysical Research Letters*, *14*(1), 29–32.

Power, W. L., & Tullis, T. E. (1991). Euclidean and fractal models for the description of rock surface roughness. *Journal of Geophysical Research: Solid Earth*, *96*(B1), 415–424. doi: 10.1029/90JB02107

Preca Trapani, R., Gabriel, A.-A., Marchandon, M., Wu, B., Palgunadi, K. H., Yen, M.-H., & Cotton, F. (2025). *Seissol input files for kahramanmaraş dynamic rupture scenarios.* Zenodo. Retrieved from `https://doi.org/10.5281/zenodo.17193784` doi: 10.5281/zenodo.17193784

Ramos, M. D., Thakur, P., Huang, Y., Harris, R. A., & Ryan, K. J. (2022). Working with dynamic earthquake rupture models: A practical guide. *Seismological Society of America*, *93*(4), 2096–2110. doi: 10.1785/0220220022

Reitman, N. G., Briggs, R. W., Barnhart, W. D., Hatem, A. E., Jobe, J. A. T., DuRoss, C. B., … Akçiz, S. (2023). Rapid surface rupture mapping from satellite data: The 2023 kahramanmaraş, turkey (türkiye), earthquake sequence. *The Seismic Record*, *3*(4), 289–298. Retrieved from `https://doi.org/10.1785/0320230029` doi: 10.1785/0320230029

Reitman, N. G., Briggs, R. W., Barnhart, W. D., Jobe, J. A., DuRoss, C. B., Hatem, A. E., ... Collett, C. M. (2023, June). *Fault rupture mapping of the 6 February 2023 Kahramanmaraş, Türkiye, earthquake sequence from satellite data (ver. 1.1, February 2024).* U.S. Geological Survey data release. (Version 1.1, updated February 2024) doi: 10.5066/P985I7U2

Ren, C., Wang, Z., Taymaz, T., Hu, N., Luo, H., Zhao, Z., ... Ding, H. (2024). Supershear triggering and cascading fault ruptures of the 2023 kahramanmaraş, türkiye, earthquake doublet. *Science*, *383*(6680), 305–311. Retrieved from https://doi.org/10.1126/science.adi1519 doi: 10.1126/science.adi1519

Renard, F., Voisin, C., Marsan, D., & Schmittbuhl, J. (2006). High resolution 3d laser scanner measurements of a strike-slip fault quantify its morphological anisotropy at all scales. *Geophysical Research Letters*, *33*(4). doi: 10.1029/2005GL025038

Rice, J. R. (1992). Chapter 20 fault stress states, pore pressure distributions, and the weakness of the san andreas fault. In B. Evans & T. fong Wong (Eds.), *Fault mechanics and transport properties of rocks* (Vol. 51, p. 475-503). Academic Press. Retrieved from https://www.sciencedirect.com/science/article/pii/S0074614208628351 doi: 10.1016/S0074-6142(08)62835-1

Rice, J. R., Sammis, C. G., & Parsons, R. (2005). Off-fault secondary failure induced by a dynamic slip pulse. *Bulletin of the Seismological Society of America*, *95*(1), 109–134. doi: 10.1785/0120030166

Rodgers, A. J., Pitarka, A., Pankajakshan, R., Sjögreen, B., & Petersson, N. A. (2020). Regional-scale 3d ground-motion simulations of m w 7 earthquakes on the hayward fault, northern california resolving frequencies 0–10 hz and including site-response corrections. *Bulletin of the Seismological Society of America*, *110*(6), 2862–2881. Retrieved from https://doi.org/10.1785/0120200147 doi: 10.1785/0120200147

Rodriguez-Marek, A., & Bray, J. D. (2006). Seismic site response for near-fault forward directivity ground motions. *Journal of Geotechnical and Geoenvironmental Engineering*, *132*(12), 1611–1620. doi: 10.1061/(ASCE)1090-0241(2006)132:12(1611)

Rosakis, A., Abdelmeguid, M., & Elbanna, A. (2025). Near-field evidence for early supershear rupture of the m w 7.8 kahramanmaraş earthquake in turkey. *Nature Geoscience*, *18*(6), 534–541. Retrieved from https://doi.org/10.1038/s41561-025-01707-2 doi: 10.1038/s41561-025-01707-2

Roten, D., Olsen, K., Day, S., Cui, Y., & Fäh, D. (2014). Expected seismic shaking in los angeles reduced by san andreas fault zone plasticity. *Geophysical Research Letters*, *41*(8), 2769–2777. doi: 10.1002/2014GL059411

Savage, H. M., & Brodsky, E. E. (2011). Collateral damage: Evolution with displacement of fracture distribution and secondary fault strands in fault damage zones. *J. Geophys. Res. Solid Earth*, *116*(B3), 405–419. doi: 10.1029/2010JB007665

Schliwa, N., Gabriel, A.-A., & Ben-Zion, Y. (2025). Shallow fault zone structure affects rupture dynamics and ground motions of the 2019 ridgecrest sequence to regional distances. *Journal of Geophysical Research: Solid Earth*, *130*(6), e2025JB031194. Retrieved from https://agupubs.onlinelibrary.wiley.com/doi/abs/10.1029/2025JB031194 doi: https://doi.org/10.1029/2025JB031194

Shahi, S. K., & Baker, J. W. (2011). An empirically calibrated framework for including the effects of near-fault directivity in probabilistic seismic hazard analysis. *Bulletin of the Seismological Society of America*, *101*(2), 742–755. doi: 10.1785/0120100090

Shahi, S. K., & Baker, J. W. (2014). An efficient algorithm to identify strong-velocity pulses in multicomponent ground motions. *Bulletin of the Seismological Society of America*, *104*(5), 2456-2466. doi: https://doi.org/10.1785/0120130191

Shi, Z., & Day, S. M. (2013). Rupture dynamics and ground motion from 3-d rough-fault simulations. *Journal of Geophysical Research: Solid Earth*, *118*. doi: 10.1002/jgrb.50094

Somerville, P. G., Smith, N. F., Graves, R. W., & Abrahamson, N. A. (1997). Modification of empirical strong ground motion attenuation relations to include the amplitude and duration effects of rupture directivity. *Seismological Research Letters*, *68*(1), 199–222. Retrieved from `https://doi.org/10.1785/gssrl.68.1.199` doi: 10.1785/gssrl.68.1.199

Spudich, P., & Chiou, B. S. (2008). Directivity in nga earthquake ground motions: Analysis using isochrone theory. *Earthquake Spectra*, *24*(1), 279–298. doi: 10.1193/1.2928225

Spudich, P., & Frazer, L. N. (1984). Use of ray theory to calculate high-frequency radiation from earthquake sources having spatially variable rupture velocity and stress drop. *Bulletin of the Seismological Society of America*, *74*(6), 2061–2082. doi: 10.1785/BSSA0740062061

Strasser, F. O., Abrahamson, N. A., & Bommer, J. J. (2009). Sigma: Issues, insights, and challenges. *Seismological Research Letters*, *80*(1), 40–56. doi: 10.1785/gssrl.80.1.40

Strasser, F. O., & Bommer, J. J. (2009, October). Review: Strong ground motions—have we seen the worst? *Bulletin of the Seismological Society of America*, *99*(5), 2613–2637. Retrieved from `https://doi.org/10.1785/0120080300` doi: 10.1785/0120080300

Styron, R., & Pagani, M. (2020). The gem global active faults database. *Earthquake Spectra*, *36*(1_suppl), 160–180. doi: 10.1177/8755293020944182

Suppe, J. (2014). Fluid overpressures and strength of the sedimentary upper crust. *Journal of Structural Geology*, *69*, 481-492. Retrieved from `https://www.sciencedirect.com/science/article/pii/S0191814114001552` (Fluids and Structures in Fold and Thrust Belts with Recognition of the Work of David V. Wiltschko) doi: https://doi.org/10.1016/j.jsg.2014.07.009

Taufiqurrahman, T., Gabriel, A.-A., Ulrich, T., Valentová, L., & Gallovič, F. (2022). Broadband dynamic rupture modeling with fractal fault roughness, frictional heterogeneity, viscoelasticity and topography: The 2016 mw 6.2 amatrice, italy earthquake. *Geophysical Research Letters*, *49*(22), e2022GL098872. doi: https://doi.org/10.1029/2022GL098872

Tinti, E., Casarotti, E., Ulrich, T., Taufiqurrahman, T., Li, D., & Gabriel, A. (2021). Constraining families of dynamic models using geological, geodetic and strong ground motion data: The Mw 6.5, October 30th, 2016, Norcia earthquake, Italy. *Earth and Planetary Science Letters*, *576*, 117237. doi: 10.1016/j.epsl.2021.117237

Türker, E., Yen, M.-H., Pilz, M., & Cotton, F. (2023, October). Significance of pulse-like ground motions and directivity effects in moderate earthquakes: The example of the mw 6.1 gölyaka-düzce earthquake on 23 november 2022. *Bulletin of the Seismological Society of America*, *114*(2), 955–964. Retrieved from `https://doi.org/10.1785/0120230043` doi: 10.1785/0120230043

Ulrich, T., Gabriel, A.-A., Ampuero, J.-P., & Xu, W. (2019). Dynamic viability of the 2016 mw 7.8 kaikōura earthquake cascade on weak crustal faults. *Nature communications*, *10*(1), 1213.

Uphoff, C., Rettenberger, S., Bader, M., Madden, E. H., Ulrich, T., Wollherr, S., & Gabriel, A.-A. (2017). Extreme scale multi-physics simulations of the tsunamigenic 2004 sumatra megathrust earthquake. In *Proceedings of the international conference for high performance computing, networking, storage and analysis* (pp. 1–16). Denver, Colorado: ACM. doi: 10.1145/3126908.3126948

Vallée, M., Landès, M., Shapiro, N. M., & Klinger, Y. (2008). The 14 november 2001 kokoxili (tibet) earthquake: High-frequency seismic radiation originating from the transitions between sub-rayleigh and supershear rupture velocity regimes. *Journal of Geophysical Research: Solid Earth*, *113*(B7). doi: 10.1029/2007JB005520

Vyas, J. C., Gabriel, A.-A., Ulrich, T., Mai, P. M., & Ampuero, J.-P. (2023). How does thermal pressurization of pore fluids affect 3d strike-slip earthquake dynamics and ground motions? *Bulletin of the Seismological Society of America*, *113*(5), 1992–2008. doi: 10.1785/0120220205

Vyas, J. C., Galis, M., & Mai, P. M. (2024). Ground-motion variability for ruptures on rough faults. *Bulletin of the Seismological Society of America*, *114*(2), 965–981. doi: 10.1785/0120230117

Wessel, P., Luis, J. F., Uieda, L., Scharroo, R., Wobbe, F., Smith, W. H. F., & Tian, D. (2019). The generic mapping tools version 6. *Geochemistry, Geophysics, Geosystems*, *20*(11), 5556–5564. doi: 10.1029/2019GC008515

Withers, K. B., Olsen, K. B., Day, S. M., & Shi, Z. (2019). Ground motion and intraevent variability from 3d deterministic broadband (0–7.5 hz) simulations along a nonplanar strike-slip fault. *Bulletin of the Seismological Society of America*, *109*(1), 229–250. Retrieved from `https://doi.org/10.1785/0120180006` doi: 10.1785/0120180006

Withers, K. B., Olsen, K. B., Shi, Z., & Day, S. M. (2019). Validation of deterministic broadband ground motion and variability from dynamic rupture simulations of buried thrust earthquakes. *Bulletin of the Seismological Society of America*, *109*(1), 212–228. doi: 10.1785/0120180005

Wollherr, S., Gabriel, A., & Mai, P. M. (2019). Landers 1992 “reloaded”: Integrative dynamic earthquake rupture modeling. *Journal of Geophysical Research: Solid Earth*, *124*(7), 6666–6702. doi: 10.1029/2018JB016355

Wollherr, S., Gabriel, A.-A., & Uphoff, C. (2018). Off-fault plasticity in three-dimensional dynamic rupture simulations using a modal discontinuous galerkin method on unstructured meshes: implementation, verification and application. *Geophysical Journal International*, *214*(3), 1556–1584. doi: 10.1093/gji/ggy213

Wu, B., Li, B., Zhang, H., Huang, S., Li, G., & Gabriel, A.-A. (2025). Near-fault strong-motion of the 2023 mw7.8 kahramanmaraş earthquake: Insights into high-frequency radiation mechanisms. *Journal of Geophysical Research: Solid Earth*, *130*(11). Retrieved from `https://agupubs.onlinelibrary.wiley.com/doi/abs/10.1029/2025JB031757` doi: https://doi.org/10.1029/2025JB031757

Wu, F., Xie, J., An, Z., Lyu, C., Taymaz, T., Irmak, T. S., … Zhou, B. (2023). Pulse-like ground motion observed during the 6 february 2023 mw7. 8 pazarcık earthquake (kahramanmaraş, se türkiye). *Earthquake Science*, *36*(4), 328–339. doi: https://doi.org/10.1016/j.eqs.2023.05.005

Yao, S., & Yang, H. (2023). Towards ground motion prediction for potential large earthquakes from interseismic locking models. *Earth and Planetary Science Letters*, *601*, 117905. doi: 10.1016/j.epsl.2022.117905

Yeh, T.-Y., & Olsen, K. B. (2024). Simulation of 0–7.5 hz physics-based nonlinear ground motions for maximum credible earthquake scenarios at the long valley dam, ca. *Earthquake Spectra*, *40*(2), 1479–1506. doi: https://doi.org/10.1177/87552930231226135

Yen, M., von Specht, S., Lin, Y., Cotton, F., & Ma, K. (2021, 09). Within- and between-event variabilities of strong-velocity pulses of moderate earthquakes within dense seismic arrays. *Bulletin of the Seismological Society of America*, *112*(1), 361-380. Retrieved from `https://doi.org/10.1785/0120200376` doi: 10.1785/0120200376

Yen, M.-H., Türker, E., Ulrich, T., Marchandon, M., Gabriel, A.-A., & Cotton, F. (2025). An analysis of directivity pulses using empirical data and dynamic rupture simulations of the 2023 kahramanmaras earthquake doublet. *Earthquake Spectra*, 1–20. doi: 10.1177/87552930241305012

Zhao, C., Mia, M. S., Elbanna, A., & Ben-Zion, Y. (2024). Dynamic rupture modeling in a complex fault zone with distributed and localized damage. *Mech. Mater.*, *198*, 105139.

Supporting Information for "Do 3D Dynamic Rupture Models Capture the Variability in Long-Period Velocity Pulses? Insights from the 2023 M_w 7.8 Kahramanmaraş Earthquake"

Rachel Preca Trapani[1], Mathilde Marchandon[1], Kadek Hendrawan Palgunadi[3,4], Baoning Wu[2], Ming-Hsuan Yen[5], Fabrice Cotton[5], Alice-Agnes Gabriel[2,1]

[1]Department of Earth and Environmental Sciences, Ludwig-Maximilians-Universität (LMU), Munich, Germany

[2]Scripps Institution of Oceanography, UC San Diego, La Jolla, CA, USA

[3]Swiss Seismological Service (SED), ETH Zürich, Switzerland

[4]Department of Geophysical Engineering, Institut Teknologi Sepuluh Nopember, Indonesia

[5]GFZ, Helmholtz Centre, Potsdam, Germany

Contents of this file

Corresponding author: R. Preca Trapani, Department of Earth and Environmental Sciences, Ludwig-Maximilian-Universität, Munich, Theresienstraße 41, Munich, 80333, Germany. (R.Preca@lmu.de)

Additional Supporting Information (Files uploaded separately)

1. Movies S1 and S2

Introduction

This supplementary material includes a table describing the 1D velocity model used in this study (Table S1) and a table defining the computational costs and mesh sizes of the models used in this study (Table S2). This supplementary material also includes supplementary figures S1 - S8. Figure S1 shows examples of the extracted pulse signals during the pulse extraction method. Figure S2 compares the pulse map from the pulse analysis applied to the model from Jia et al. (2023), as depicted in Yen et al. (2025), to the reference model described in this study. Figure S3a further explains the initial stress orientation field, whilst Figure S3b shows a rupture speed fault output for a special case from the waviness model in which supershear rupture speeds were reached. Figure S4 shows the relative prestress ratio, $\mathcal{R}$, Figure S5 is the same plot as Figure 9 but showing a comparison to the observed ground motion data, and Figure S6 shows the Fourier spectra of the models. Figures S7 and S8 show the pulse analysis applied to the different cases from the fracture network simulations. The corresponding captions to the separately included movies can also be found in this file.

Captions of Supplementary Movies

Movie S1: Evolution of absolute slip rate (m/s) for all six dynamic rupture models explored in this study.

Movie S2: Evolution of dynamic rupture speed (m/s) for all six dynamic rupture models explored in this study.

References

Gabriel, A.-A., Garagash, D. I., Palgunadi, K. H., & Mai, P. M. (2024). Fault size–dependent fracture energy explains multiscale seismicity and cascading earthquakes. *Science*, *385*(6707), eadj9587. doi: 10.1126/science.adj9587

Güvercin, S. E., Karabulut, H., Konca, A. O., Doğan, U., & Ergintav, S. (2022). Active seismotectonics of the east anatolian fault. *Geophysical Journal International*, *230*(1), 50–69. doi: https://doi.org/10.1093/gji/ggac045

Jia, Z., Jin, Z., Marchandon, M., Ulrich, T., Gabriel, A.-A., Fan, W., ... Fialko, Y. (2023, 08). The complex dynamics of the 2023 kahramanmaraş, turkey, mw 7.8-7.7 earthquake doublet. *Science (New York, N.Y.)*, *381*, eadi0685. doi: https://doi.org/10.1126/science.adi0685

Shahi, S. K., & Baker, J. W. (2014). An efficient algorithm to identify strong-velocity pulses in multicomponent ground motions. *Bulletin of the Seismological Society of America*, *104*(5), 2456-2466. doi: https://doi.org/10.1785/0120130191

Yen, M.-H., Türker, E., Ulrich, T., Marchandon, M., Gabriel, A.-A., & Cotton, F. (2025). An analysis of directivity pulses using empirical data and dynamic rupture simulations of the 2023 kahramanmaras earthquake doublet. *Earthquake Spectra*, 1–20. doi: 10.1177/87552930241305012

Depth [km]	Density [kg m^{-3}]	c_s [km/s]	c_p [km/s]
1.0	2465.0	2.43	4.52
2.0	2640.2	3.03	5.62
4.0	2665.2	3.31	5.75
6.0	2685.3	3.38	5.85
8.0	2708.1	3.43	5.96
10.0	2716.7	3.44	6.00
12.0	2727.5	3.46	6.05
16.0	2789.0	3.62	6.32
20.0	2808.3	3.67	6.40
25.0	2920.1	3.92	6.83
30.0	2936.8	3.94	6.89
37.0	3221.2	4.40	7.80
45.0	3370.6	4.56	8.22
1000.0	3400.2	4.61	8.3

Table S1. Description of the 1D velocity model adapted from Güvercin et al. (2022) that we use in our models.

Model	CPUh	Mesh Size [elements]
Model 1	10,590.0	31,452,737
Model 2	8,778.8	31,452,737
Model 3	10,680.0	52,370,578
Model 4	9,033.9	31,452,737
Model 5	8,873.8	31,452,737
Model 6	9,400.0	52,294,408

Table S2. Computational cost in CPU hours (CPUh) of all six 3D dynamic rupture models explored in this study, as well as the size of the associated computational mesh. Models 1, 2, 4, and 5 use the same computational mesh, whereas Models 3 and 6 use different meshes that incorporate the different fault roughness explored in each. All simulations are performed on 48 nodes with 48 CPUs of the supercomputer SuperMUC-NG. The computational cost is calculated as [CPUh] = [number of nodes] × [number of CPUs per node] × [computing time (hours)]

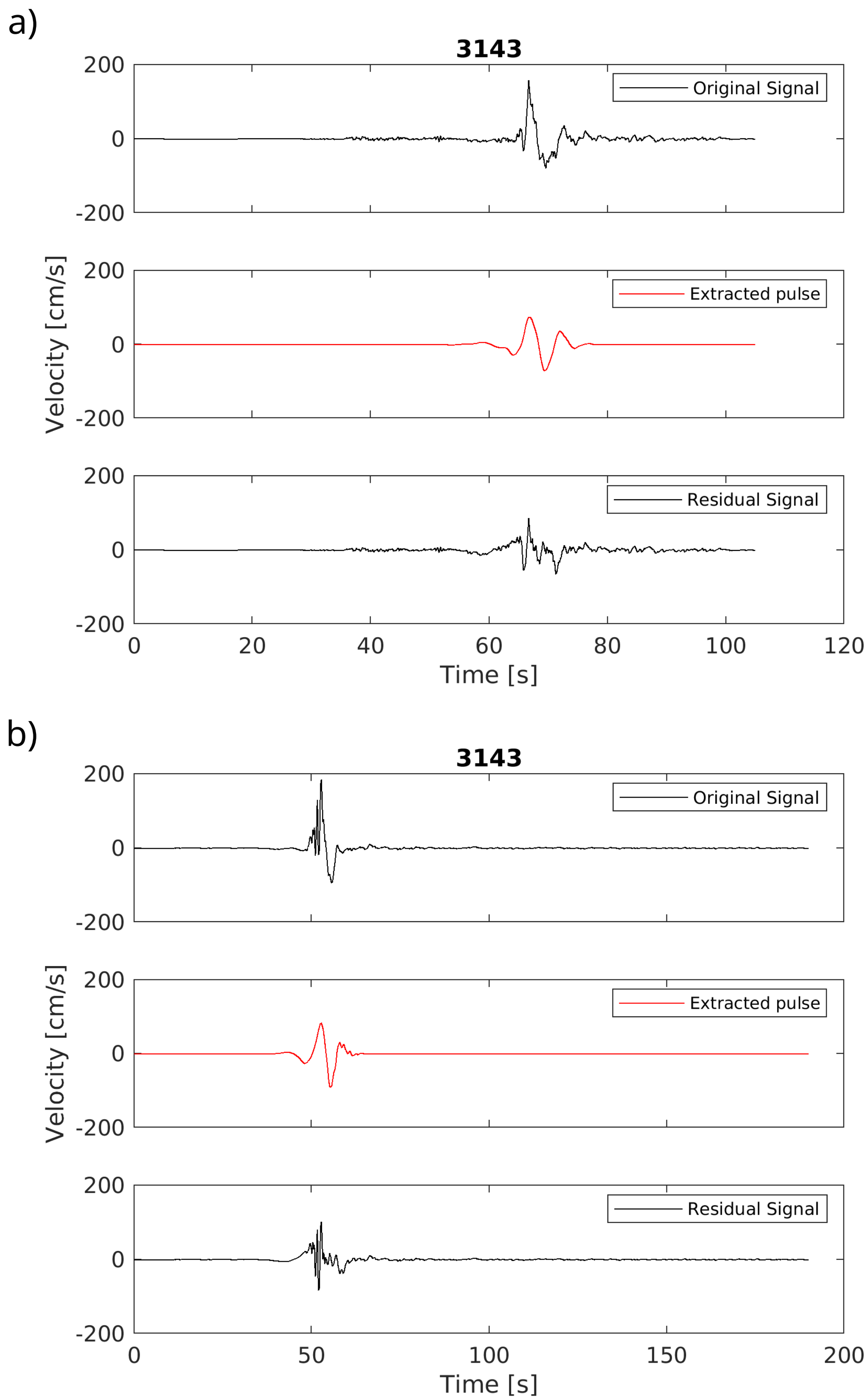

Figure S1. An example of the original signal generated during the pulse extraction method of Shahi and Baker (2014), the extracted pulse and the residual signal for station 3143 for a) the observational data and b) the reference model.

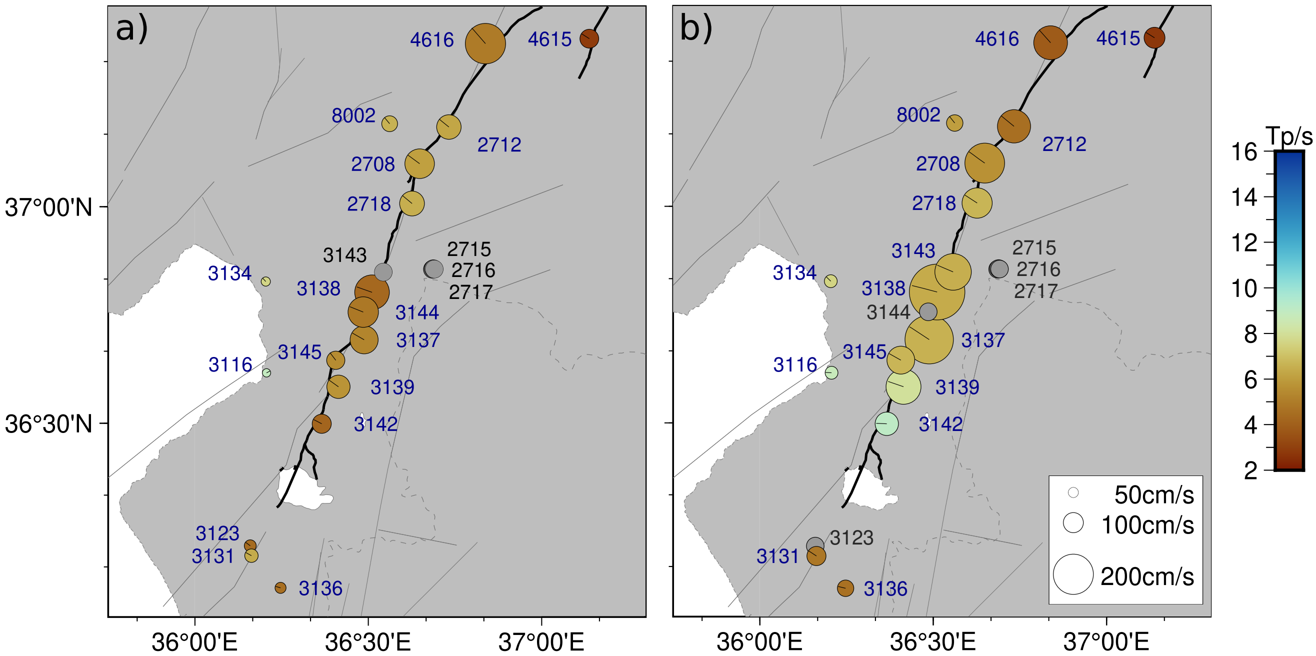

Figure S2. Comparison of the pulse maps for a) the Jia et al. (2023) model, as shown in Figure 1b and b) the reference model, as seen in Figure 8a. There are some minor differences between a) and Figure 3a of Yen et al. (2025), such as slight variations in the precise pulse property values from the pulse analysis. This is mainly due to differences in operating systems and software versions. However, there is a notable difference in the pulse orientation for station 3116 and the negative classification of station 3143 as pulse-like here in a). These differences could be due to different approaches to the pre-processing of the synthetic data before applying the pulse analysis. In this study, no pre-processing is applied to the signals prior to the pulse analysis, whereas the signals were trimmed in the Yen et al. (2025) study. A change in total signal length can strongly influence the energy ratios used for the pulse criterion calculations, which are necessary for the Shahi and Baker (2014) pulse extraction method.

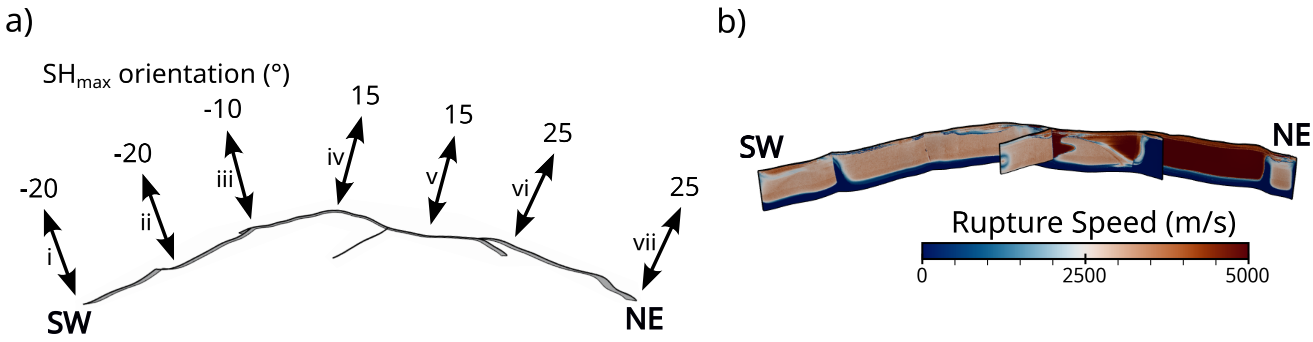

Figure S3. a) Distribution of SHmax orientations along the fault for the reference model. All models except for Model 3 follow this setup. b) A special case for Model 6 where the change in the $\mathcal{R}$ value results in supershear rupture speeds along the eastern portion of the EAF.

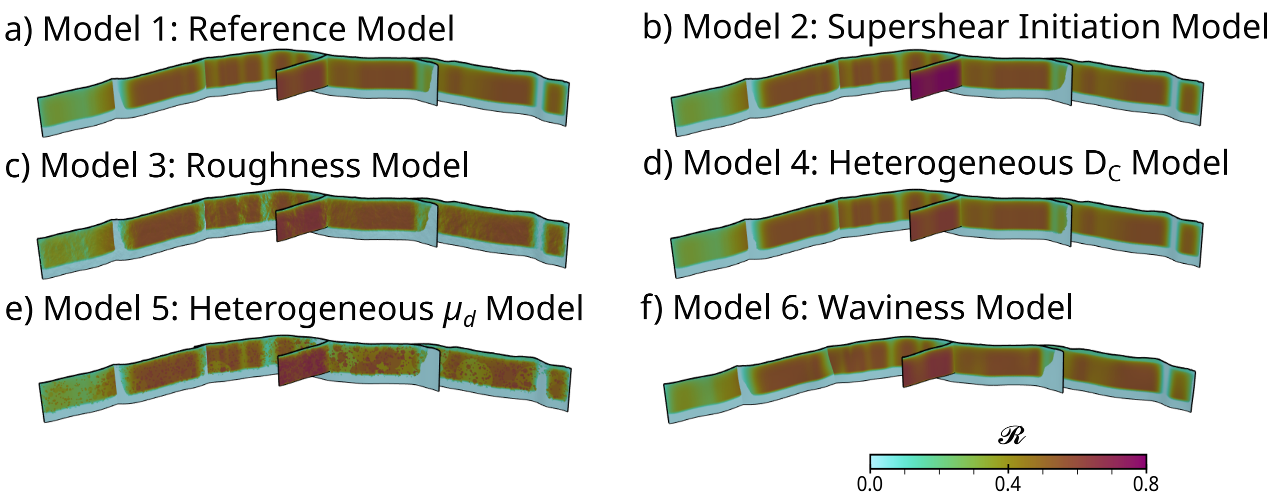

Figure S4. Relative prestress ratio ($\mathcal{R}$) for the six dynamic rupture models analysed in this study. Variations in $\mathcal{R}$ relative to the reference model (a) appear in Model 2: the supershear initiation model (b), which shows a higher $\mathcal{R}$ value along the NPF, Model 3: multi-scale roughness (c), Model 5: heterogeneous μ_d (e), and Model 6: large-scale waviness (f). Model 4: heterogeneous D_c (d) has a relative prestress ratio identical to that of the reference model.

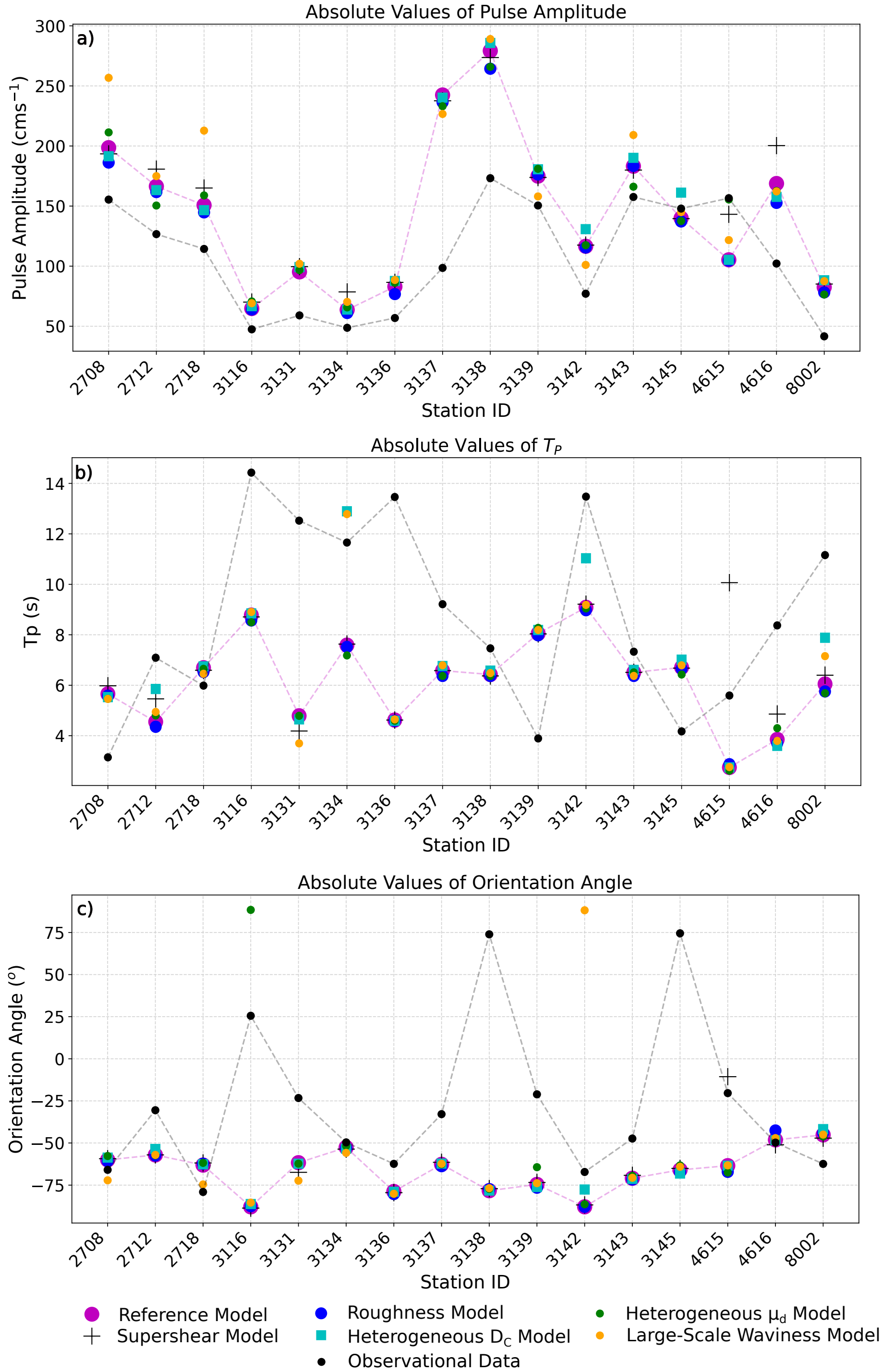

Figure S5. Comparison of a) pulse amplitude, b) pulse period (Tp), and c) pulse orientation variability for all six models and the observational data, similar to Figure 7. The pink dotted line highlights the reference model and the black dotted line highlights the observational data to better compare the variability of the models with the observational data.

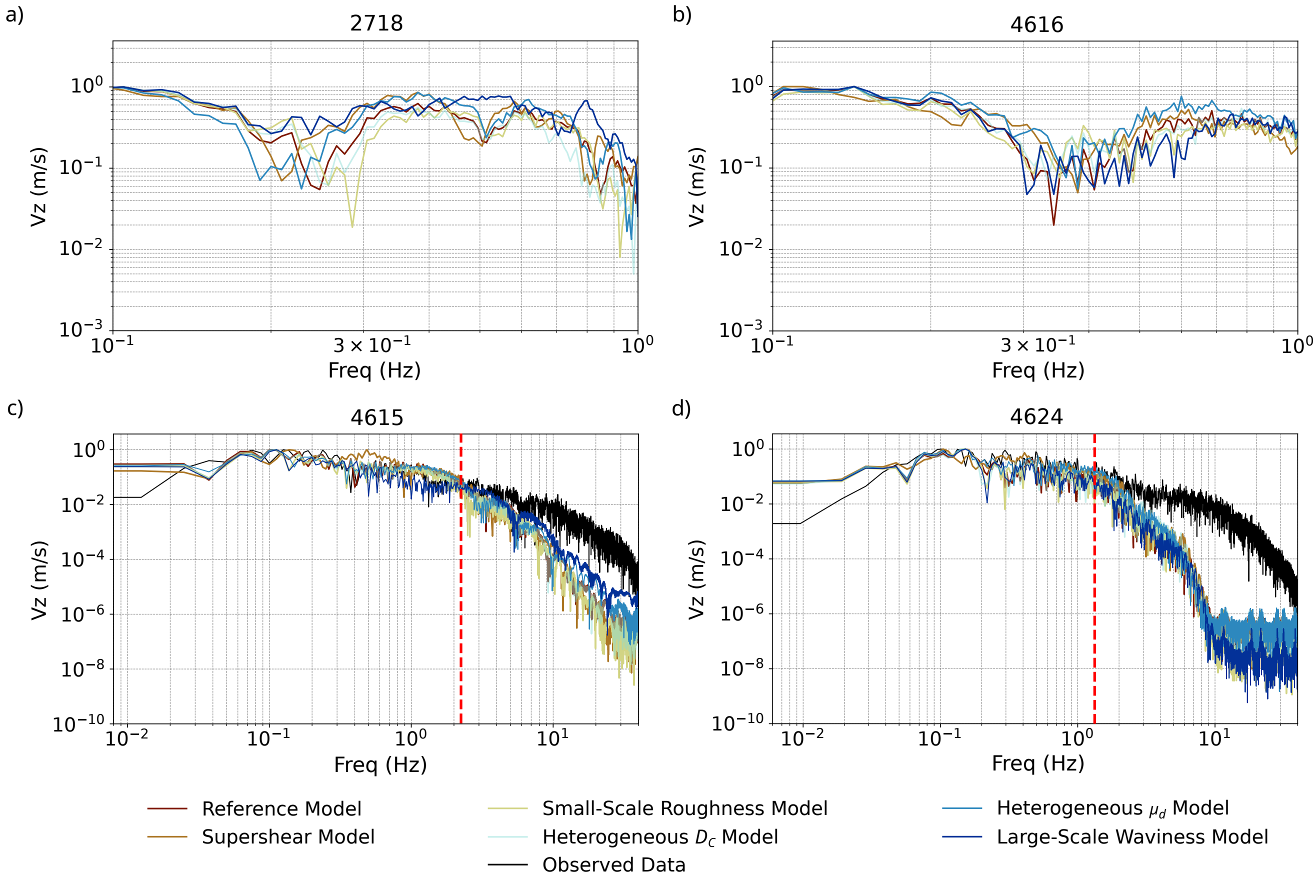

Figure S6. Fourier spectra of the six models and observational data. a) and b) are the spectra for the six synthetic models at two very near-fault stations (2718 and 4616) up to 1 Hz, the resolved frequency of the models. c) and d) are the spectra for the six models and the observational data up to 40 Hz. Station 4615 is a very near-fault station, whereas station 4624 is located 10 km away from the EAF. The red dotted lines depict the fall-off frequency.

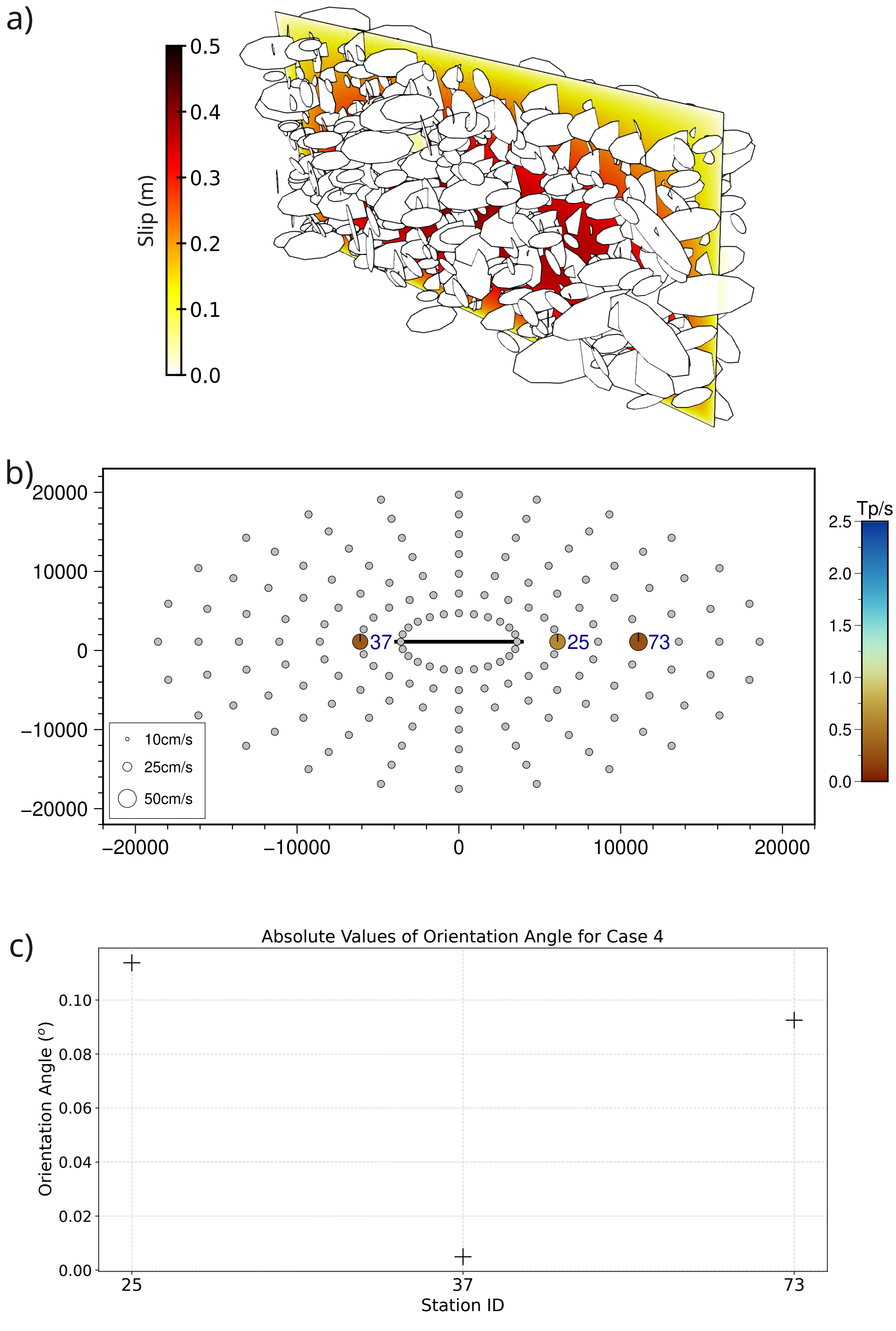

Figure S7. a) Fracture network setup and accumulated slip for case 4 from Gabriel et al. (2024), b) pulse map showing all the stations considered and c) pulse orientation for the three stations classified as impulsive for case 4.

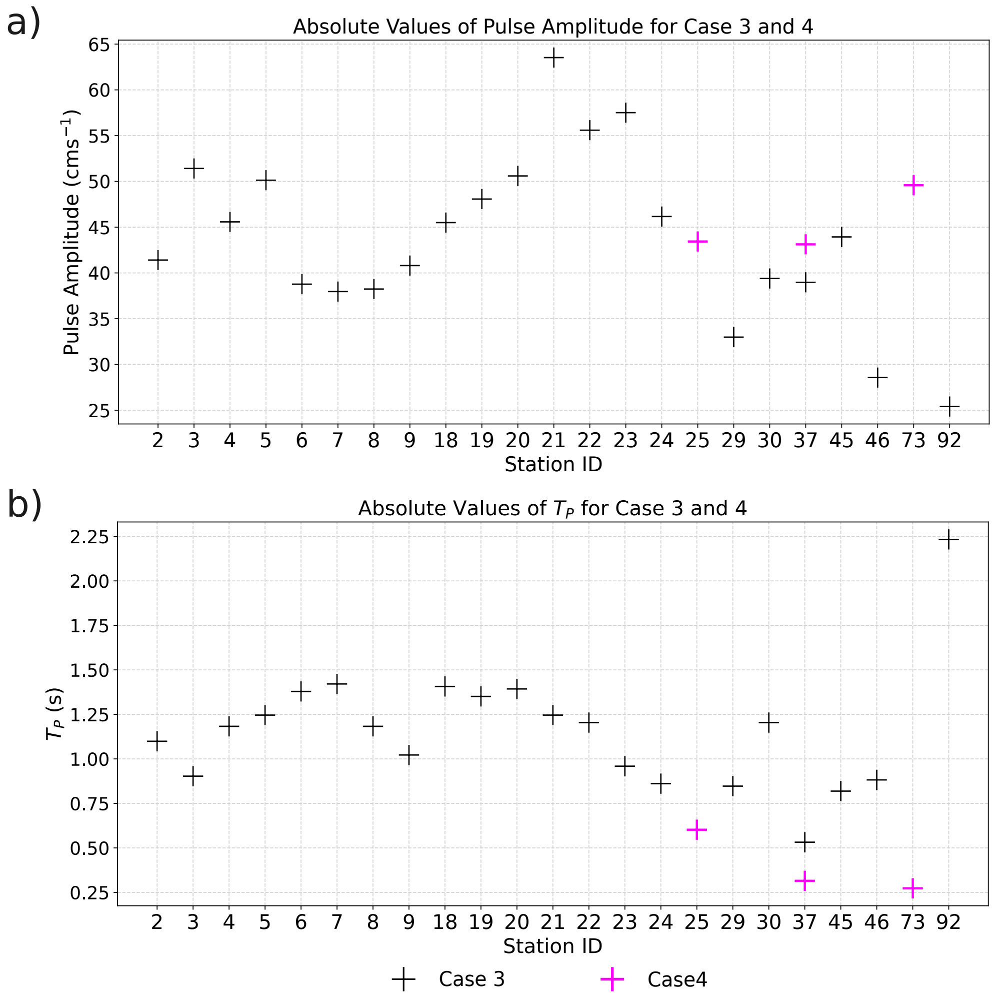

Figure S8. Comparison of a) pulse amplitude and b) T_p for case 3 and case 4 for the fracture network setup of Gabriel et al. (2024).